A computational fluid dynamics (CFD) based method for assessing the hydrodynamic impact of animal borne data loggers on host marine mammals

Kyte, Adam; Pass, Christopher; Pemberton, Richard; Sharman, Matthew; McKnight, J. Chris

Published in:
Marine Mammal Science

DOI:
10.1111/mms.12540

Publication date:
2019

Document version:
Peer reviewed version

2019-04

A Computational Fluid Dynamics (CFD) Based Method for Assessing the Hydrodynamic Impact of Animal Borne Data Loggers on Host Marine Mammals

Kyte, A

10.1111/mms.12540
Marine Mammal Science
Wiley

Title

A Computational Fluid Dynamics (CFD) Based Method for Assessing the Hydrodynamic Impact of Animal Borne Data Loggers on Host Marine Mammals.

Authors

Adam Kyte*, Christopher Pass, Richard Pemberton, Matthew Sharman.

DesignFlow, Reynolds Building, Plymouth University, Drake Circus, Plymouth. PL4 8AA. UK.

J. Chris McKnight

Sea Mammal Research Unit (SMRU), Scottish Oceans Institute, University of St Andrews, St Andrews, Fife, KY16 8LB. UK.

*Corresponding Author: Adam Kyte, DesignFlow, Reynolds Building, Plymouth University, Drake Circus, Plymouth. PL4 8AA.

Email: adam.kyte@plymouth.ac.uk.

Abstract

Animal-borne data loggers (ABDLs) or "tags" are regularly used to elucidate animal ecology and physiology, but current literature highlights the need to assess associated deleterious impacts including increased resistive force to motion. Previous studies have used Computational Fluid Dynamics (CFD) to estimate this impact, but many suffer limitations (*e.g.*, inaccurate turbulence modeling, neglecting boundary layer transition, neglecting added mass effects, and analyzing the ABDL in isolation from the animal).

A novel CFD-based method is presented in which a "tag impact envelope" is defined utilizing simulations with and without transition modelling to define upper and lower drag limits, respectively, and added mass coefficients are found *via* simulations with sinusoidally varying inlet velocity, with modified Navier-Stokes conservation of momentum equations enforcing a shift to the animal's noninertial reference frame. The method generates coefficients for calculating total resistive force for any velocity and acceleration combination, and is validated against theory for a prolate spheroid. An example case shows ABDL drag impact on a harp seal of 11.21% - 16.24%, with negligible influence on added mass.

By considering the effects of added mass and boundary layer transition, the approach presented is an enhancement to the CFD-based ABDL impact assessment methods previously applied by researchers.

Key Words

ABDL, Added Mass, Animal-Borne Data Loggers, Bio-logging, Boundary Layer Transition, CFD, Computational Fluid Dynamics, Hydrodynamics, Tag, Telemetry.

Nomenclature

$\boldsymbol{a}$ = Acceleration (m/s^2)

$\boldsymbol{A}$ = Amplitude of sinusoidal velocity oscillation (m/s)

$\boldsymbol{C_d}$ = *Drag Coefficient*

$\boldsymbol{C_{d\_u}}$ = Drag Coefficient of untagged animal based on untagged animal wetted area

$\boldsymbol{C_{d\_t}}$ = Drag Coefficient of tagged animal based on untagged animal wetted area

$\boldsymbol{C_m}$ = *Added Mass Coefficient*

$\boldsymbol{C_{m\_u}}$ = Added Mass Coefficient of untagged animal

$\boldsymbol{C_{m\_t}}$ = Added Mass Coefficient of tagged animal

$\boldsymbol{f}$ = Frequency of sinusoidal velocity oscillation (Hz)

$\boldsymbol{F}$ = Total resistive force *OR* Required Thrust Force (N)

$\boldsymbol{g_x}$ = Gravitational acceleration vector in the x-direction (m/s^2)

$\boldsymbol{m}$ = Total mass of animal (kg)

$\boldsymbol{V}$ = Total volume of displaced water (m^3)

$\boldsymbol{Re}$ = Reynolds Number based on total animal length

$\boldsymbol{Re_x}$ = Local Reynolds Number (based on distance along body measured from nose / leading edge)

$\boldsymbol{S}$ = Untagged animal wetted area (m^2)

$\boldsymbol{t}$ = Time (seconds)

$\boldsymbol{u_{in}}$ = Instantaneous inlet velocity (m/s)

u_{mean} = Mean velocity (m/s)

u = Velocity in x-direction (m/s)

v = Velocity in y-direction (m/s)

w = Velocity in z-direction (m/s)

x = Cartesian coordinate axis aligned with longitudinal axis of animal (m)

y = Cartesian coordinate axis perpendicular to longitudinal axis of animal in vertical direction (m)

z = Cartesian coordinate axis perpendicular to longitudinal axis of animal in horizontal direction (m)

φ = Phase (Radians)

ρ = Density of Seawater at 10^{o}C (kg/m^{3})

μ = Dynamic viscosity of seawater (Pa.s)

Introduction

Externally mounted animal-borne data loggers (ABDLs or ''tags'') are utilized across a range of ecological disciplines to understand how animals exploit their environment and also to guide conservation efforts (Fig. 1). Despite offering clear research benefits (McMahon *et al*. 2007), it has been shown that there can be a significant impact on the subject animal as a consequence of tag attachment (Wilson *et al*. 1986, Culik and Wilson 1991, Culik *et al*. 1994, Boyd *et al*. 1997, Ropert-Coudert *et al*. 2007*a*, Bowlin *et al*. 2010, Saraux *et al*. 2011, Rosen *et al*. 2018). In the short term, energetic and behavioral changes may occur (Chipman *et al*. 2007). In the long term, the effect of an increase in drag force, and the subsequent increase in the Cost of Transport (COT), have been identified as having potential population level effects on some tagged animals (Saraux *et al*. 2011).

In the context of marine animals, possible consequences of increased drag are alterations in diving behavior and energetics (Ropert-Coudert *et al*. 2007*b*, Maresh *et al*. 2014). During periods when an animal cannot select slower swim speeds to offset tag induced increases in drag, particularly during prey pursuit, power output must be increased (Wilson *et al*. 2002). For example Culik *et al*. (1993) found that tagged Adelie penguins (*Pygoscelis adeliae*) increased power output by 24% over untagged animals. Increased power output may not be sustainable; into the medium and long term, subject animals may adjust their behavior to compensate for device effects. Hull (1997) observed changes in foraging trip duration, swim speed, and breeding behavior in little penguins (*Eudyptula minor*), while Ropert-Coudert *et al*. (2007b) showed that tagged little penguins performed fewer foraging dives with more time spent at depth. Further, experimental work on rigid animal models conducted by multiple authors (Bannasch *et al*. 1994, Watson and Granger 1998, Wilson *et al*. 2004, Todd Jones *et al*. 2013) demonstrates substantial, measurable increases in hydrodynamic drag.

While studies employing ABDL allow researchers otherwise unachievable levels of insight into the behavior of free ranging animals, the utility of such devices must be weighed against the ethical considerations surrounding these deleterious impacts. While the number of studies employing tags has increased substantially over the preceding 2 – 3 decades (McMahon *et al*. 2011, Vandenabeele *et al*. 2011), the number of papers aiming to identify and minimize ABDL impact has not (Vandenabeele *et al*. 2011). This is concerning and highlights the pressing need for more work in this area (McIntyre 2015). Aside from the obvious and important ethical considerations surrounding ABDL use, there is the practical problem of introducing biases into ABDL generated data sets. Addition of an ABDL may alter the behavior being measured (Wilson and Vandenabeele 2012, Rosen *et al*. 2018); therefore, work to improve ABDL designs and reduce device impact becomes of multifaceted significance.

Experimental methods to minimize the deleterious tag impact have been presented by Bannasch *et al*. (1994), where incremental improvement of a given tag design was made through a trial and error process. However, this approach is time consuming, costly, and resource intensive.

It is also possible that a simple hydrodynamic drag increase measurement will not yield a truly representative snapshot of tag impact. The total resistive force (or perhaps more intuitively the thrust an animal must generate at any given time), is a function of instantaneous speed, direction of motion and acceleration.

Equation 1 (Vogel 1994) describes the forces opposing animal motion. The naming convention given in Equation 1 for each of these force components is used throughout the remainder of this paper. Equation 1 shows that, at a constant velocity, the animal must overcome only hydrodynamic drag but when accelerating, for example during prey pursuit or predator evasion, additional inertial forces give rise to the 'acceleration reaction' force; the sum of the forces required both to accelerate the mass of the animal body forwards (the body mass force) *and* to accelerate the fluid displaced by the animal backwards, otherwise known as the added mass force. The added mass force is likely to be a considerable component of the total resistive force for bodies accelerating rapidly through a comparatively dense fluid such as water and, as discussed by Vogel (1994), has been shown to be significant for a range of biological organisms.

$$\overbrace{F = \underbrace{\frac{1}{2} C_d \rho S u^2}_{\text{Hydrodynamic Drag}} + \underbrace{C_m \rho V a}_{\text{Added Mass Force}}}^{\text{Acceleration Reaction Force}} + \underbrace{ma}_{\text{Body Mass Force}} \qquad \text{(1.)}$$

Total Hydrodynamic Force

Total Resistive Force

The body mass force is given by Newtons 2nd Law and, assuming dimensional similarity between experiment and the subject animal, wind tunnel tests could demonstrate, at a given speed, the increase in hydrodynamic drag caused by a tag. Such approaches, however, are limited in their ability to determine whether the presence of the tag has any impact on the added mass component of the acceleration reaction.

Practical experimental constraints often mean that an animal model is held stationary while flow is driven over the body. At a constant velocity, the animal is in an inertial frame of reference and this approach is equivalent to the real case in which the *animal* is moving rather than the fluid. During acceleration this equivalence no longer holds, the animal is now in a noninertial frame of reference and simply accelerating the flow over a stationary animal will not accurately capture the

inertial effect of the added mass[1]. Lamb (1932) and Newman (1977) present calculated C_m values for a range of idealized shapes that can serve as reasonable estimates for many bodies, however, these values are based on potential, or inviscid, flow theory and so neglect the complexities induced by viscous effects in a real fluid. They may also be limited in their ability to predict the impact of an irregular shaped tag on the added mass force.

Numerical modelling has the potential to estimate device effects without the need for experiments, before prototyping or manufacturing has occurred, by conducting 'virtual experiments' in which fluid flow over a tagged animal is simulated using Computational Fluid Dynamics (CFD) software.

Such tools can be used not only to predict the hydrodynamic drag increase imposed by a tag but also to predict its effect on the added mass component of the acceleration reaction force. The required switch from an inertial to a noninertial frame of reference, while holding the animal body stationary, can be achieved through the inclusion of an additional body force, applied to all of the fluid within the simulation domain. This is implemented by a user-defined source term (S_x) in the Navier-Stokes equation for conservation of momentum in the direction of flow; assuming flow in the x direction this is stated by equation 2.

$$\boldsymbol{\rho\left(\frac{\partial u}{\partial t}+u\frac{\partial u}{\partial x}+v\frac{\partial u}{\partial y}+w\frac{\partial u}{\partial z}\right)=-\frac{\partial p}{\partial x}+\mu\left(\frac{\partial^2 u}{\partial x^2}+\frac{\partial^2 u}{\partial y^2}+\frac{\partial^2 u}{\partial z^2}\right)+\rho g_x+S_x} \quad \textbf{(2.)}$$

$$\textit{Where } \boldsymbol{S_x=\rho\frac{du_{in}}{dt}}$$

This approach directly includes the inertial effects present in the noninertial frame and is thus truly representative of a moving animal in stationary fluid.

Computational studies may offer a significant benefit over traditional experimental methods; driving design improvement efforts, while reducing the requirement for animal testing. However, whilst many CFD software packages allow a novice user to obtain a result, considerable skill is required to select and apply an appropriate modelling method which will generate reliable and physically realistic results. Using the example of a Sea Mammal Research Unit (SMRU) GPS phone tag mounted on a free-swimming adult female harp seal (*Pagophilus groenlandicus*) (Fig. 2), predictions of drag penalty induced by the tag at a constant speed are compared for three different CFD methods. A methodology is then developed for predicting C_m of both the tagged and untagged animal. Results presented allow estimates of hydrodynamic drag and acceleration reaction force to be made for any combination of instantaneous velocity and rate of acceleration within a defined range. This work demonstrates the sensitivity of results to the methodology applied, offers researchers insight into

1 Note that the discussion of the key physics given here is limited in scope and detail for overall clarity. More detail on the points raised can be found in the supplementary material provided.

scenarios in which tag impact is likely to be most significant and also details a practical means by which tag impact can be estimated for those engaged in the design and/or deployment of ABDL.

Computational Fluid Dynamics Basic Theory

Computational Fluid Dynamics (CFD) methods[2] calculate flow variables according to the fundamental physical laws requiring conservation of mass and momentum[3]; laws expressed by the Navier-Stokes equations. A marine mammal CFD study would begin by creating a virtual bounding box containing the animal body geometry. This computational domain must be discretized into a "mesh" of thousands/millions of individual finite volumes (or "elements"). Boundary conditions and key physical parameters such as inlet flow velocity, turbulence intensity, and fluid properties are then applied, allowing flow variables to be computed for each finite volume in an iterative process. Iterations continue until they converge towards a solution that satisfies the governing equations. It is important to note that this process only offers an *approximation* of real world flows. The quality of any results generated depends on the *degree* of approximation made in 3 areas;

1. Geometric approximations/simplifications.
2. Meshing/discretization.
3. Applied physics.

1). Geometric simplifications are often required to make mesh generation practical. In marine mammal modelling, this may include removing eyes, vibrissae, and flippers. While some simplifications may have only a negligible impact on results, others may be more detrimental. Some simplifications are unavoidable; for example the mesh refinement required to model very small scale morphological features (such as vibrissae) will almost certainly be impractical, so the analyst must remain aware that this could be affecting results. Ultimately, the degree of geometric simplification that is deemed acceptable may be informed by the aim of the study; if, for example, the aim is simple flow pattern prediction then a higher degree of simplification may be acceptable than if reliable numerical data are required.

2). Meshing/discretization errors arise as the continuous variation of flow variables across the domain, described by the governing equations, is approximated. Such errors are governed by both the *type* of mesh element employed and the *resolution* of the mesh. 3D mesh elements are typically hexahedral or tetrahedral. While tetrahedral meshes are generally relatively easy to generate, they are computationally inefficient and the inherent lack of alignment with any dominant flow direction can induce error (known as numerical diffusion) in results. Hexahedral meshes are therefore desirable despite the increased user skill and workload involved during preparation.

2 While a range of CFD methods/tools are available, this work focuses only on the application of the commonly used Finite Volume CFD method.
3 It can also be necessary to consider conservation of energy, especially in cases where heat transfer is a significant consideration.

3). Simplification of the specified physics (for example in turbulence and boundary layer transition treatment) can also induce error. The choice of animal movement / swimming mode is also an important consideration. While modelling a rigid body in a single fixed 'gliding' position clearly offers a computationally convenient simulation approach, the resistive force imposed on an actively swimming animal is likely to be influenced significantly by the motion of the body and its effect on the flow-field. As a consequence, steps should be taken to model the physics of the real process as closely as practically possible. However, CFD modelling of bodies in which animal shape and velocity are dynamically changing would increase the complexity and computational expense of simulations by orders of magnitude, possibly rendering such an approach impractical.

Turbulent flows are characterized by complex and unsteady spatial and temporal variations in flow velocity driven by the formation of vortices of a range of length scales (Pope 2000). Modelling the behavior of each of these vortices using a method known as Direct Numerical Simulation (DNS) would be the ideal methodology, but is impractical because the mesh resolution required imposes an intractable computational expense. So we must ask "what is the impact on the accuracy of results when we deviate from this ideal?"

One approximation is to consider velocity at a given point as the sum of an average and time varying component, a process which gives rise to the Reynolds Averaged Navier-Stokes (RANS) equations (Pope 2000). This significantly simplifies the approach by predicting the average *effect* of turbulent vortices *without directly modelling* them by using a turbulence model. The most widely used turbulence models are based on the calculation of an 'eddy viscosity', an artificial viscosity that accounts for turbulent energy dissipation.

The two-equation k–ε model (where k is turbulent kinetic energy and ε is rate of turbulent kinetic energy dissipation (Pope 2000) is commonly used. Despite its widespread use, there are problems associated with this model in cases where reliable boundary layer modelling is necessary. Problems are three-fold; first, the eddy viscosity is assumed to be isotropic *i.e.*, the same length scale in all directions and second, damping functions are used to approximate the boundary layer velocity profile (Menter 1994). Thirdly, since a fully turbulent boundary layer is assumed, no prediction of boundary layer transition is possible. Its accuracy is therefore severely limited where boundary layer behavior is important; flow separation can be markedly under-predicted and, in extreme cases, not predicted at all (Menter 2011). The k–ε model is therefore not suitable for cases requiring reliable modelling of viscous drag *or* boundary layer separation; both key requirements in animal and tag modelling respectively.

Despite these issues, a number of authors have applied the k–ε model in tag impact studies. Hazekamp *et al.* (2010) conducted a CFD study of tag induced effects on a simplified gray seal (*Halichoerus grypus*) model, comparing results for both tagged and untagged animals to estimate a drag impact of around 12% while Balmer *et al.* (2014) assessed the drag

sensitivity of a cetacean dorsal fin to the location of a single-pin transmitter. An improvement in near-wall modelling is offered by the RNG k–ε model, a modified version of the standard k–ε model. This method was applied by Pavlov *et al*. (2007) and Pavlov and Rashad (2012) in the design of dolphin dorsal fin tags.

Boundary layer modelling can be significantly improved by using the Shear Stress Transport (SST) model, a k–ε /k–ω hybrid, where ω is the turbulent frequency (Menter 1993). The k–ω model is used in the near-wall region to directly model the boundary layer velocity profile (rather than applying damping functions) (Menter 1994), significantly improving separation prediction. However, the k–ω model suffers from accuracy problems in the free-stream (Menter 1993) so, at some distance from a surface, a switch is made to the more robust k–ε model. Despite these improvements, the SST model is still subject to the assumptions of an isotropic eddy viscosity and a fully turbulent boundary layer. This approach would therefore *under-predict* the impact of a tag if located in a region where the boundary layer would naturally be laminar without the presence of the tag.

Significant uncertainty appears to surround the likely boundary layer transition location on many marine mammals. According to data presented by Hoerner (1965), in terms of an idealized smooth axisymmetric streamlined shaped body, below Re_x of approximately $1x10^5$ the boundary layer may be predominantly laminar. The proportion of turbulent boundary layer increases with Re until, at a value between approximately $5x10^6$ and $1x10^7$, it is likely to be almost entirely turbulent. Fish *et al*. (1988) observed harp and ringed (*Pusa hispida*) seals swimming at *Re* between $0.77x10^6$ and $1.79x10^6$ and Williams and Kooyman (1985) observed typical swim speeds in harbor seals (*Phoca vitulina*) corresponding to a Re range of $1.1x10^6$ to $2.6x10^6$, implying that significant portions of laminar boundary layer could be present.

In reality, animal bodies such as seals deviate significantly from the ideal form. Eyes, mouths, and vibrissae are all morphological features easily capable of inducing a turbulent boundary layer over most of the animal length regardless of Reynolds Number. However, synthetic compliant skin inspired by the naturally compliant skin of a dolphin may delay boundary layer transition (Gaster 1998), suggesting that some animals could also possess highly developed drag reduction mechanisms. This uncertainty is highlighted in the literature; Stelle *et al.* (2000) demonstrated predominantly turbulent boundary layer flow over Steller sea lions (*Eumetopias jubatus*) at *Re* from $5x10^6$ to $6x10^6$ while Rohr *et al.* (1998) used bioluminescence experiments to predict boundary layer transition at the blowhole on a dolphin swimming at *Re* $5.1x10^6$, clearly representing a significant amount of laminar boundary layer flow.

Reliable boundary layer transition prediction is therefore essential when predicting the hydrodynamic drag of the animal body and the net hydrodynamic drag increase imposed by an ABDL. An ABDL constitutes a major surface imperfection, so if located far forward enough to be in an otherwise naturally laminar portion of the boundary layer it will certainly force transition; the drag increase will be the hydrodynamic drag of the tag *plus* the associated additional viscous drag due to the

increased proportion of turbulent boundary layer over the animal skin/fur/feather/carapace. Neglecting this additional viscous drag by assuming a fully turbulent boundary layer (a common CFD approach) would *under predict* the impact of a tag.

The simulation methodology can be more closely aligned with reality by coupling the SST model with a boundary layer transition model. The γ transition model developed by Menter *et al*. (2015) is used in the current study. This model solves a single transport equation for the turbulent intermittency γ, in combination with experimentally derived correlations in order to trigger boundary layer transition onset. Such models, however, are typically tuned to give reliable results in specific situations, leading to potential error in cases that differ significantly from those for which they have been calibrated.

Shorter *et al.* (2014) assessed the hydrodynamic forces acting on three different tag shapes, validated against water tunnel experiments; boundary layer transition is modelled. Fiore *et al*. (2017) continued this work, again applying the k–ε model to assess multiple derivatives of an initial tag design.

Another issue is the lack of consideration of transient (*i.e*., time varying) flow forces induced by the tag. Highly unsteady flow patterns can form in the wake of a bluff body (Bearman 1997), imposing a fluctuating force on the tag (and thus on the animal). The example of uniform flow past a circular cylinder illustrates this point. Across certain ranges of Re, an unsteady wake is a formed by alternate shedding of vortices from the cylinder surface at the boundary layer separation points, causing fluctuations in drag force and cross-force. In some cases, such forces could be sufficient to induce discomfort or even tissue damage in tagged animals (Walker *et al.* 2012). Previous studies appear to often enforce steady flow, thus neglecting transient effects.

In summary, our literature review found no studies using the SST model (or other methods capable of comparable boundary layer prediction) combined with appropriate laminar to turbulent boundary layer transition modelling. No single study was found assessing the impact of a tag on a full animal body including consideration of boundary layer transition and unsteady or transient flow effects. Furthermore, previous studies do not appear to account for additional forces arising due to acceleration. As a consequence, the possible impact of a tag on the added mass force (and therefore on the thrust an animal must develop to achieve a required speed) has received little attention.

It must be noted that DNS and eddy viscosity based models represent respectively only the most complex and most accessible modelling approaches. Other approaches are available including Large Eddy Simulation (LES) and Detached Eddy Simulation (DES), offering improvements over eddy viscosity models but simplifications over DNS (Pope 2000). However, the computational expense of such methods is likely to render them impractical for tag impact/development studies. This

paper seeks to define an approach that allows researchers to estimate the full impact of a tag on a subject animal using eddy viscosity based turbulence models

Methods

Sensitivity to Turbulence Model Selection

In order to quantify the influence of turbulence model selection on the predicted hydrodynamic drag and tag impact, simulations of an untagged adult female harp seal, swimming at a fixed velocity of 1.3 m/s, were conducted using three different methods (Table 1). Method 1 represents our closest practical approximation of the real physics and is therefore deemed to be the "Baseline" to which the other methods are compared. Each simulation was then repeated with the geometry including a SMRU GPS phone tag (Fig. 2).

Hydrodynamic Drag Variation with Glide Velocity

Method 1 was then used to predict the hydrodynamic drag imposed at glide speeds across the range 0.9 m/s to 1.7 m/s. Fixed velocity simulations using both the tagged and untagged animal were conducted in 0.2 m/s increments as per Table 2. The minimum and maximum swim speeds selected were based on data obtained from wild deployment of a Little Leonardo W1000-PD3GT sensor mounted on a free ranging harp seal during February 2015 (Fig. 3 shows a representative 120 s extract of the speed sensor data provided).

Results yield an equation of the form given at equation 3 and can be used to predict C_d and therefore the hydrodynamic drag component of the total resistive force at any instantaneous glide velocity within the described velocity range.

$$C_d = xRe^{-n} \tag{3.}$$

Prediction of the Added Mass Component of the Acceleration Reaction Force

In order to model the required switch from an inertial to a noninertial reference frame and thereby capture the added mass component of the total hydrodynamic force, simulations (for both tagged and untagged cases) were conducted with a sinusoidally varying inlet velocity (equation 4). While a real animal does not swim with a sinusoidal velocity variation, application of a velocity varying in this way provides a convenient means by which to determine C_m as there is an analytical solution for acceleration which can be used to define the body force required to shift to a noninertial frame of reference. This additional body force was defined *via* the inclusion of a source term (equations 5 and 6) in the conservation of momentum equation in the direction of flow (as per equation 2). The predicted C_m may then subsequently be used to calculate the added mass force for any real, nonsinusoidal, velocity variation.

$$u_{in} = Asin(2\pi ft + \varphi) + u_{mean} \quad (4.)$$

$$a = \frac{du_{in}}{dt} = 2\pi f[Acos(2\pi ft + \varphi)] \quad (5.)$$

$$S_x = \rho a \quad (6.)$$

Typical maximum and minimum animal swim speeds of 1.5 m/s and 1.1 m/s, with an approximate maximum acceleration of 0.871 m/s^2 were identified as broadly representative of real animal behavior based on provided speed sensor data (extract shown at Fig. 3). Values of A=0.2 m/s, u_{mean} = 1.3 m/s and f = 0.693 Hz have therefore been selected to yield representative velocities and accelerations in equations 4 and 5. φ was set to ensure that simulations started from the minimum velocity occurring across the sinusoidal cycle (1.1 m/s).

It should again be stressed that the use of a sinusoidally fluctuating velocity (and associated sinusoidally varying body force) has been used only as a means of determining the correct value for C_m, and does not assume that this is the way the real animal velocity is expected to vary with time. The approach of determining C_m values in this way has been validated against published C_m data for a prolate spheroid with a fineness ratio of 5. Newman (1977) states an expected C_m of 0.06 based on potential, or inviscid, flow theory while our numerical simulations of the same shape yield a mean C_m of approximately 0.064, an increase of 6.66% over the published value[4].

Note that all simulation work conducted in this paper uses seawater and, consequentially, does not assume inviscid flow. It is therefore likely that the difference between published and simulated C_m is due to the boundary layer and wake present in all real cases. This additional force component is the Bassett Force, a history term that accounts for noninstantaneous, temporal changes in wake and boundary layer state that occur as velocity changes (Fackrell 2011).

The tagged and untagged animal simulations yield the total hydrodynamic force, *i.e.*, the total resistive force as per equation 1 *minus* the body mass force required to accelerate the mass of the animal. The body mass force is not present in the CFD model because the volume representing the animal is massless in the simulations. By rearranging equation 1, equations 7 and 8 were then used to determine C_{m_t} and C_{m_u} respectively, utilizing the derived equations of the form of Equation 3 to determine C_{d_t} and C_{d_u}.

$$C_{m\_t} = \frac{F - (\frac{1}{2} C_{d\_t} \rho S u^2)}{\rho V a} \quad (7.)$$

$$C_{m\_u} = \frac{F - (\frac{1}{2} C_{d\_u} \rho S u^2)}{\rho V a} \quad (8.)$$

[4] For more information on the prolate spheroid validation work conducted refer to the supplementary material provided.

The C_m and C_d values predicted using the above process may then be used to estimate the force experienced by an animal across any combination of velocity and acceleration (*i.e.*, at any given instantaneous velocity and acceleration, irrespective of the fact that it will not be varying sinusoidally).

Geometry Generation and Meshing

The 3D model of the seal body was produced (using Rhinoceros 5.0 and Solidworks 2014 CAD software) from an existing 3D photogrammetric model developed at the SMRU, St. Andrews. The model is a free-swimming adult in glide phase, housed in the captive animal facility at the University of Tromsø, Norway (McKnight 2018). The animal is 1.85 m long and 0.44 m wide, with an x-distance from animal nose to the front of the tag base of 0.25 m. The computational domain extends 5 animal lengths upstream, above, below and either side of the animal, and 15 animal lengths downstream. Fully hexahedral meshes generated using ANSYS ICEM CFD V18 were used in all simulations (Fig. 4). Best practice guidelines in meshing for SST-γ have been followed as per Langtry and Menter (2006) and Menter *et al*. (2015).

Modelling Assumptions

1. The animal is assumed to be hydrodynamically smooth and rigid; small morphological features including eyes, fur, and vibrissae have been removed and are therefore not modelled.
2. The tag is assumed perfectly aligned with the incident flow and located (as per wild deployments) at the base of the skull on the ventral surface of neck. Details such as antennae ribs have been removed from the tag geometry.

Boundary Conditions, Setup and Solver

Tables 3 and 4 detail the assumed environmental and boundary conditions. All simulations used ANSYS CFX V18 to solve the discretized RANS equations. ANSYS (2009) present information on the formulation of the turbulence and transition models applied.

Fully transient simulations were conducted in all cases, utilizing an adaptive time-stepping scheme with parameters set to achieve a residual convergence target of 1×10^{-5} within 5 coefficient loops. All simulations were run using a single compute node on Plymouth University's High Performance Computing (HPC) facility, comprising 16 Intel Xeon E5-2683 processors with 128GB RAM.

Simulation Reliability Checks

A full mesh dependency study was undertaken on a baseline domain extending 5 animal lengths upstream, above, below and either side of the animal, and 15 animal lengths downstream in order to ensure that results presented are independent of the level of mesh refinement. The tagged animal model was used as the basis for this study, Table 5 details the levels of mesh resolution applied and the associated simulation results. Note that while the predicted hydrodynamic drag varies by only around 1.1% between simulations 1 and 4 (which covers an approximate 6 fold increase in number of mesh nodes[5]) there is an increase in predicted tag drag of 22.7%. This demonstrates the importance of looking deeper than just 'top level' simulation outputs when assessing mesh dependency. Measurement of only total drag would, in this case, suggest that a mesh of 3.75×10^6 nodes would be adequate. This would lead to a marked under prediction of tag drag and therefore would markedly reduce the predicted tag impact. All subsequent results presented in this study were obtained using the mesh applied in simulation 3, using 20.5×10^6 nodes.

In addition, a full domain dependency study has been conducted by first halving and then quartering the baseline distance from the animal body to each domain boundary. Table 6 details the corresponding simulation results which indicated that the solution appears to be relatively insensitive to domain size with a variation in total drag force of around 1.3% between the baseline and smallest domains. The original baseline domain was used to generate all subsequent results presented in this paper.

Results

Sensitivity to Turbulence Model Selection

Table 7 presents drag predictions for the untagged animal. As expected, the SST-γ simulation gives the lowest drag prediction because it permits the boundary layer on some regions of the animal surface to remain laminar. Table 8 presents hydrodynamic drag predictions (both measured force and C_d) for the tagged animal, comparing drag to that of the untagged animal for each method. The predicted drag increase induced by the tag varies from 16.24% to 2.25% between modelling methods, showing that results are highly sensitive to turbulence/transition model selection.

Figure 5 breaks total drag values down into pressure and viscous components for both animal body and the tag itself (where fitted), showing where the differences between methods arise. Key observations are:

5 Note that mesh refinements made from run 1 to run 2 are focused around the body and wake of the animal (hence a large overall increase in the number of mesh nodes). Refinements from run 2 to runs 3 and 4 are made local to the tag, so whilst element size is significantly reduced in the vicinity of the tag, there is a comparatively small increase in overall number of nodes.

- The SST-γ model predicts a viscous drag that is 46% and 49% lower in the untagged case than the SST only and k-ϵ models respectively.
- The SST-γ model predicts that addition of a tag causes an increase in viscous drag on the animal itself of 11.52% over the comparable untagged case.
- Pressure drag is a substantial proportion of total drag in all cases (Based on untagged animal results it constitutes; SST-γ 48%, SST 36%, k-ϵ 29%) and is highly sensitive to the turbulence / transition modelling approach adopted.
- Tag viscous drag is negligible in all cases.

Figure 6 shows skin friction coefficient (C_f) distribution for untagged/tagged cases, comparing SST-γ and SST only cases. C_f is a nondimensional measure of viscous drag and so provides a useful means by which to visualize boundary layer transition. A sudden increase to relatively high C_f (as seen immediately aft of the fore flipper bulges and also in the wake of the tag in Fig. 6b) is indicative of transition onset. Fig. 8 compares the velocity in the region surrounding the tag for k-ϵ and SST-γ cases, highlighting the difference in predicted wake formation.

Hydrodynamic Drag Variation with Glide Velocity

Figure 7 shows the variation in predicted C_d (and therefore the hydrodynamic drag component of the total resistive force) with *Re* based on the series of fixed velocity simulations conducted using the baseline method. The results yield equations 9 and 10 for the untagged and tagged animal respectively. The % increase in C_d induced by the tag remains relatively constant across the range of *Re* simulated, reducing from 16.74% at $Re = 2.31 \times 10^6$ down to 15.03% at $Re = 1.22 \times 10^6$. Note that in all cases C_{d_t} and C_{d_u} are based on the wetted area of the *untagged* animal.

$$\boldsymbol{C_{d\_u} = 0.0569 Re^{-0.166}} \quad (9.)$$

$$\boldsymbol{C_{d\_t} = 0.0472 Re^{-0.143}} \quad (10.)$$

Figure 7 also compares simulated results with experimental data from Williams and Kooyman (1985). Deceleration and tow tests were used to derive C_d values for two animals with results indicating a wide range of predicted C_d values. Simulation results appear in reasonable agreement with comparable results derived from deceleration tests; however, C_d values predicted from results of tow tests are markedly higher.

Prediction of the Added Mass Component of the Acceleration Reaction Force

Figures 9a. to 9c. show results of simulations conducted using the sinusoidal inlet velocity and additional body force implemented in order to capture the added mass component of the acceleration reaction force for the purpose of identifying C_m. Results are given for a 3-second time period and show:

- Figure 9a: Simulated velocity and acceleration profiles (as defined by equations 4 and 5 respectively). Figure 9b: The variation with time of the predicted hydrodynamic drag (calculated using C_d values determined from equations 9 and 10) and the total hydrodynamic force (from simulation results). Figure 9c: C_{m_t} and C_{m_u} calculated from equations 7 and 8 respectively using the results presented at Figure 9b, showing almost identical C_{m_t} and C_{m_u} values across the velocity / acceleration cycle.

Some key observations are:

- During acceleration, the total hydrodynamic force increases significantly over the instantaneous hydrodynamic drag.
- At peak acceleration, hydrodynamic drag accounts for just 35% and 38% of total hydrodynamic force for the untagged and tagged animal respectively, the remainder being due to the added mass force. Results also show that the presence of the tag results in an increase in the maximum total hydrodynamic force of approximately 5.3% increase over the untagged case.

Discussion

Comparison of Baseline Results with Published Experimental Data

Substantially different solutions to the same fundamental problem are clearly possible simply by adopting different turbulence/transition modelling approaches. It is therefore important to validate results and assess potential sources of error, but, in the case of marine animals there is substantial uncertainty in available experimental validation data.

The untagged baseline (SST-γ) drag of 8.19N yields a C_{d_u} of 0.0052; 30% greater than the often cited value of 0.004 for seals given by Vogel (1994). This value is based on experimental work conducted by Williams and Kooyman (1985) in which deceleration and tow tests are conducted on two harbor seals (1 adult and 1 juvenile). Measured C_d varied from 0.004 to 0.010 dependent on the type of test conducted. They attribute this variation to a range of factors including the possible influence of the test equipment and also small movements in the animal's body during tests. Figure 7 also shows that results from towing tests are higher for both subject animals than the comparable deceleration tests. Whilst the current simulation results lie within the range of predictions made by Williams and Kooyman (1985) based on deceleration tests, it

is likely that simply stating a single C_d is an over-simplification of reality. Rather a single animal may well present a whole range of C_d if we could reliably measure the imposed drag force under a range of body orientations and motion types. This uncertainty means that any simulation work conducted on an animal in a single position represents only a single point in a range of drag forces experienced by a swimming seal. Also, comparisons of tag impact *are only valid under comparable conditions, i.e.*, if tagged animal simulation results are compared to results generated using the same animal in its untagged state.

Comparison of Simulated Results

The following points are revealed by inspection of Figures 5 and 6:

1. For both untagged and tagged cases, SST-γ predicts much lower viscous drag than SST and k–ε. This is due to the ability of SST-γ to model regions of laminar flow over the animal surface, rather than assuming the entire boundary layer is turbulent. Comparison between Figures 6a and 6c clearly shows the laminar (darker colored) areas on the neck and shoulder region of the seal model predicted by SST-γ.
2. For the tagged case, SST-γ predicts an increase in viscous drag on the animal surface compared to the untagged case. This is due to the tag causing transition to a turbulent boundary layer on the animal surface in the wake of the tag (seen in Fig. 6b); this region remains laminar in the untagged case (Fig. 6a). This highlights the importance of considering tag and animal together, rather than conducting simulations/experiments of the tag in isolation when making drag assessments.
3. Predicted pressure drag on the animal body is substantial in all cases. Simulations suggest some flow separation on the posterior region of the animal, fore of the rear flippers (highlighted region 3 in Fig. 10), but it is likely that in reality, the animal has evolved to minimize such separation (maybe by dynamic shape changes whilst swimming, or turbulence induced by fur/pelage energizing the boundary layer to overcome local pressure gradients). Addition of a tag actually reduces pressure drag on the animal itself in the SST-γ case, most likely because the turbulent wake of the tag energizes the boundary layer on the animal, reducing downstream separation.
4. Predicted pressure drag (of both tag and animal) is strongly influenced by the selected turbulence/transition model. This is most evident in the fact that k–ε predicts very little tag pressure drag, thus predicting total tag drag to be much lower than the other methods. The drag of the tag is dominated by the pressure drag caused by flow separation in its wake. Figure 8 shows that in comparison to SST -γ, k-ε predicts flow separation much further towards the rear of the tag "hump", meaning that the wake is smaller and the force difference between upstream and downstream faces of the tag is therefore much smaller. Velocity profiles (Fig. 10) show why

different turbulence models produce such differences in flow separation prediction. Before the influence of the tag (Fig. 10 location 1), k-ϵ predicts a much 'fuller' profile than SST; the velocity at a given distance from the animal skin is much higher. Thus in the k-ϵ case, the boundary layer carries much more fluid momentum. When the boundary layer subsequently reaches a region of adverse pressure gradient such as that behind the tag "hump" (Fig. 10 location 2) or just ahead of the animal tail (Fig. 10 location 3), this fluid momentum is unrealistically high, and overcomes the retarding influence of pressure, so flow continues rearwards. In the SST case, the boundary layer carries less momentum, it cannot overcome the adverse pressure gradient and flow direction is reversed, causing a region of recirculating separated flow (highlighted in red in Fig. 10).

5. In all cases, tag viscous drag is negligible. Drag of the tag itself is dominated by pressure drag; viscous drag is small due to the relatively small tag surface area.

6. k–ϵ results may be misleading. In the k–ϵ tagged case, lack of transition modelling (acting to over-predict overall drag) is partially masked by a likely under-prediction of tag drag due to inaccurate separation prediction. At first glance, when considering overall drag, k-ϵ and SST-γ predictions for the tagged animal appear in good agreement. However, the fact that two fundamental inaccuracies may partially mutually cancel in the k-ϵ case means that the impact of the tag on the animal may be under-predicted. This shows that a k-ϵ approach is unlikely to be suitable for tag development and impact assessment; it does not adequately model the physics that is influenced by tag design and position.

Uncertainty in SST-γ results

SST-γ predicts that in the untagged case, transition will initiate downstream of the geometric disturbances provided by the flipper bulges on the side of the animal, while transition on the back appears to begin a significant distance further along the body. The two regions of turbulent flow then coalesce towards the rear of the animal. Thus the simulation indicates that the boundary layer flow is laminar over a significant proportion of the surface of the animal.

Considering that the simulated body is highly idealized (smooth, rigid and lacking any of the surface discontinuities provided by eyes, vibrissae, *etc.*), it may be the case that transition is predicted to occur further along the body than in reality. In addition, it has been the experience of the authors that use of a similar boundary layer modelling approach in other applications (human powered vehicle development, for example), transition is predicted further aft than that seen experimentally. In such examples, it is clear that use of the γ transition model in cases that differ from those for which it has been explicitly validated may cause inaccuracy; it is likely that it is over-predicting the proportion of laminar flow to some extent on the real animal.

The "true" proportion of laminar flow most probably lies somewhere between SST predictions (*i.e.*, no laminar flow) and SST-γ predictions (*i.e.*, too much laminar flow). Thus, it is recommended that ***both*** methods are employed as a matter of course to define expressions for C_d representing a "tag impact envelope"; the SST and SST-γ results representing lower and upper bounds of the real case, respectively. At a *Re* = 1.768×10^6, the SMRU GPS phone tag impact envelope is therefore predicted to have lower and upper bounds of 11.21% and 16.24%, respectively, on the hydrodynamic drag of the modelled harp seal body.

It should also be noted that whilst SST-γ has been shown to capture the key physics of interest, it should not be seen as a highly accurate approach. Aside from inaccuracies in transition location prediction, its inherent averaging of unsteady turbulence properties is known to result in inaccuracies; the wake pressure field and the true separation point (on both tag and animal) are just two areas that will carry some uncertainty. More advanced turbulence models (*e.g.*, DES or LES) may improve predictions, but their computational expense renders them impractical as tools for tag design and impact assessment.

Prediction of Tag Impact on the Hydrodynamic Drag Component of the Total Resistive Force

Table 2 details the inlet velocity and *Re* applied in the fixed velocity simulations conducted to predict the total hydrodynamic force, showing that inlet velocity (and therefore Re) increases by around 89% between the lowest speed of 0.9m/s and the maximum of 1.7m/s. Despite this significant increase in speed, tag impact remains relatively constant, increasing from around 15% at 0.9m/s (Re = $1{,}224 \times 10^6$) to 16.74% at 1.7m/s (Re=2.312×10^6); a 1.74% increase. This shows that, while drag is increasing with Re, the proportion of the hydrodynamic drag attributable to the presence of the tag varies very little.

Figure 7 also demonstrates, in part, the difficulty in stating a single C_d value when discussing the drag characteristics of an animal. C_{d_u} reduces by 10% across the range of *Re* simulated while C_{d_t} reduces by around 8.6%; therefore any discussion surrounding animal drag should reference not only C_d, but also the *Re* to which it relates.

Prediction of the Added Mass Component of the Acceleration Reaction Force

Reference to the untagged animal simulation results given in Figure 9b. shows that the total hydrodynamic force imposed on the animal during acceleration is much higher than just the hydrodynamic drag calculated using a C_{d_u} given by equation 9 (in the untagged case, at peak acceleration, the hydrodynamic drag is only 35% of the total hydrodynamic force). This clearly shows that basing animal resistive force predictions *only* on the hydrodynamic drag at a fixed speed is a significant oversimplification of reality that neglects some very important physics.

Comparing the untagged animal results to those of the tagged animal at Figure 9b indicates that the tag induces a small but measurable increase in the total hydrodynamic force across the acceleration / deceleration cycle (5.46% at maximum force values). Despite this simulated total hydrodynamic force increase, Figure 9c. shows almost identical C_{m_t} and C_{m_u} values (determined from equations 7 and 8 respectively) indicating that the presence of the tag has no measurable impact on the added mass component of the acceleration reaction force. An interesting observation is the apparent variation in C_{m_t} and C_{m_u} across the acceleration/deceleration cycle. This effect arises because as acceleration tends to zero, values for C_m calculated by equations 7 and 8 tend to infinity. However, results do show consistently and repeatably that, at peak acceleration and deceleration (*i.e.*, when the acceleration reaction force is at its greatest), $C_{m\_t} = C_{m\_u} = 0.068$. Figure 11 compares the simulated total hydrodynamic force (from Fig. 9b) with a calculated total hydrodynamic force (from equation 1) based on a fixed C_m (*i.e.*, $C_{m\_t} = C_{m\_u} = 0.068$) and the C_{d_t} and C_{d_u} from equations 10 and 9 respectively. Results show close agreement between the calculated and simulated total hydrodynamic force profiles, indicating that the assumption of a single, fixed C_m value (equal to C_m at peak acceleration) is valid. A consequence of this finding is that even in periods of high acceleration, the presence of the tag has a negligible effect on the added mass force; the impact of the tag is purely a result of the increased hydrodynamic drag (*i.e.*, the fact that C_{d_t} is higher than C_{d_u} at any given Re).

Also, the total hydrodynamic force variation predicted at Figure 9b (for both the tagged and untagged animal) does not include the body mass force and is therefore not the total resistive force that the animal must overcome. When this is considered, results presented here suggest that any increase in thrust the animal must provide to offset the effect of the tag during periods of high acceleration is likely to be a very small proportion of the overall thrust. As an example, at a velocity of 1.1 m/s an acceleration of 0.43 m/s^2 (typical of the early stages of an acceleration episode such as prey pursuit, indicated in red in Fig. 3) and an animal mass of 256.75 kg (equal to the displaced mass of water) predicted C_d and C_m values suggest that an untagged animal must produce 123.93N of thrust, compared to 124.84N for a tagged animal – a mere 0.74% increase. In contrast, for an animal moving at a constant 1.1m/s, the predictions suggest an untagged thrust requirement of 6.02N compared to a tagged thrust requirement of 6.93m/s; a 15.04% increase. Clearly, animals do not move at a constant velocity, so at any given instant, the true percentage impact of the tag is likely to lie somewhere between these two scenarios, and (for any given velocity and acceleration) can easily be calculated if C_d and C_m are known for both tagged and untagged cases.

When considering a wider simulation methodology for use in predicting the drag forces imposed on marine animals, it is clear that the approach taken must be driven by the requirements of the study being conducted. Results presented here indeed show that the acceleration reaction force is the dominant force imposed on an animal during periods of acceleration and deceleration (and therefore constitutes most of the thrust the animal must generate). Any study aiming to predict the total resistive force or, analogously, total required thrust, of an animal (with or without tag) must therefore

adopt either the approach detailed in this paper or some other equivalent means of modelling the additional forces arising due to acceleration. If, however, the aim of the study is to estimate the drag impact of the tag in order to drive the design and improvement process there is no measurable benefit to including any assessment of acceleration induced forces. This statement must, however, be caveated; the added mass component of the acceleration reaction is strongly dependent on volume and so when the volume of a tag is only a very small proportion of the volume of the animal (as is the case in this study), the effect of the tag on the acceleration reaction force is likely to be minimal or indeed unmeasurable. If however, the volume of the tag is a significant proportion of the animal volume, its effect during acceleration is likely to be more marked and this must be considered by researchers undertaking tag impact assessment studies. Based on this information it is reasonable to suggest that minimizing the tag to animal volume ratio should constitute one of the key tag design guidelines of which, according to Rosen *et al.* (2018), there are few.

Simulation Process and Associated Computing Times

Of particular use to those researchers undertaking CFD based tag design work is some consideration of the simulation process that was followed to generate the results presented in this paper. It is also important to consider the likely run time required to complete simulation work. After extensive trials with a range of different simulation strategies, the following process was found to be the most efficient and was followed both for the tagged and untagged animal:

- An initial steady state simulation was conducted with an inlet velocity equal to u_{mean} (or 1.3 m/s) in order to provide initial conditions for a fully transient simulation. Required simulation time was around 12 h.
- A fully transient, fixed inlet velocity simulation at u_{mean} was conducted to yield a baseline set of results, using an adaptive time-stepping approach to reach a well-converged solution yielding stable drag values.
- In order to predict hydrodynamic drag variation, a set of 4 further fixed velocity transient simulations were conducted as per Table 2, again using an adaptive time-stepping approach. Initial conditions for each simulation were provided using scaled baseline results; every nodal velocity from the baseline case was scaled by a factor equal to the ratio of the required velocity to the baseline case velocity (*e.g.*, 0.9/1.3 = 0.692 for the 0.9m/s simulation). Simulation times varied from around 36 hours (in the case of the untagged animal at low inlet velocities) to in excess of 350 h for the tagged animal at the highest inlet velocities. An approximate average of 175 h is a reasonable estimate. In all cases, sufficient simulation time was allowed in order to ensure a well converged, stable solution.
- A single transient simulation was conducted with the sinusoidally varying velocity inlet. This simulation was initialized from the fixed velocity results corresponding to the minimum velocity occurring across the sinusoidal cycle (in this case 1.1 m/s). This simulation took required around 140 h and 350 h for the tagged and untagged

animals respectively. Simulations were run until well converged, with negligible difference in drag between three successive sinusoidal velocity periods.

Therefore, in order to estimate tag impact at a single, fixed representative swim speed it is likely that useful results could be available after around 374 h or 15.6 days (based on 2 x 12 h steady state simulations and 2 x 175 h fixed velocity transient simulations. The additional simulations required to extend these results, not only to predict hydrodynamic drag variation but also to predict added mass coefficients, increases computer time by approximately 2,000 h (approximately a 5-fold increase based on an additional 8 fixed velocity simulations and 2 sinusoidal inlet simulations). Note that, in addition to the times estimated above, additional simulation time is required in order to develop a mesh, domain and time-step independent model before tag impact results can be considered reliable. This package of work must be completed once per animal / tag combination and could result in a minimum of 6 additional simulations depending on the process taken, so typically another 1,050 h assuming an average of 175 h per simulation

All of the above computing times assume HPC parallel processing using 16 Intel Xeon E5-2683 processors with 128GB RAM. In our experience, this is a speed-up of a factor of around 4 compared to a typical high-specification desktop machine. Computing times can be reduced by using more HPC processors, but speed-up is not proportional to number of processors and software licensing costs per processor can become prohibitive.

Conclusions

CFD, if applied appropriately, can be a powerful tool in estimating ABDL impact. Accuracy of previous studies has been limited by factors such as inappropriate turbulence modelling or consideration of a tag in isolation, neglecting the effects of the changes that the tag induces in the flow over the animal itself. An approach is presented in which CFD may be used to determine C_d (as a function of Re) and C_m for any animal (tagged or untagged). With C_d and C_m known, the total hydrodynamic force imposed on the animal at any given velocity and acceleration may be easily calculated.

The recommended approach uses SST ***and*** SST-γ methods (with appropriate checks on mesh dependency, domain dependency and transient behavior) to identify expressions for upper and lower C_d bounds respectively, forming a "tag impact envelope". This approach estimates that a SMRU GPS phone tag will increase hydrodynamic drag by 11.21% – 16.24% on the reference animal body used here. The recommended approach for prediction of C_m employs CFD simulations with sinusoidally varying inlet velocity and a user defined body force in the direction of motion to impose the required noninertial frame of reference.

This shows that for the reference animal body used here, the total hydrodynamic force imposed on an accelerating animal is much higher than that predicted by consideration only of the instantaneous hydrodynamic drag. It is also shown,

however, that the presence of the tag has no measurable impact on the added mass force. As a consequence it is recommended that (provided tag volume is a small percentage of animal volume) researchers interested primarily in estimating and reducing tag impact employ a simulation methodology that predicts tag impact at a fixed, realistic speed. Researchers interested in predicting the total resistive force imposed on an accelerating animal must, however, employ either the methodology developed here, or some analogous method, by which the additional forces arising due to acceleration can be captured.

The uncertainties highlighted throughout this paper show that CFD should not be considered a definitive prediction tool, but rather as a complementary tool to experimental work using tagged animals. A reasonable approach may be to conduct the majority of tag design and improvement work using CFD tools to identify the predicted tag impact envelope, then conduct field and/or captive animal studies during final stages of design and impact assessment. The presented approach is applicable to any study in which the subject animal, whether land, sea, or air based, is moving at sufficient speed that overcoming drag represents significant energy expenditure.

Acknowledgments

The authors would like to thank Martin Biuw, Ippie Suzuki, Mario Acquarone and Marie – Anne Blanchet for providing the speed sensor data used within this work.

References

ANSYS Inc. (2009) ANSYS CFX solver theory guide, ANSYS Inc, USA

Balmer, B.C., R.S. Wells., L.E. Howle *et al.* (2014) Advances in cetacean telemetry: A review of single-pin transmitter attachment techniques on small cetaceans and development of a new satellite-linked transmitter design. Marine Mammal Science. 30(2), 656 - 673.

Bannasch, R., R.P. Wilson and B. Culik. (1994) Hydrodynamic aspects of design and attachment of a back mounted device in penguins. Journal of Experimental Biology. 194, 83 - 96.

Bearman, P. (1997) Near wake flows behind two and three dimensional bluff bodies. Journal of Wind Engineering and Industrial Aerodynamics. 69 - 71, 33 - 54.

Bowlin, M.S., P. Henningsson., T.F. Muijres., R.H.E. Vluegels., F. Liechti., A. Hedenstrom. (2010). The effects of geolocator drag and weight on the flight ranges of small migrants. Methods in Ecology and Evolution, 1, 398–402.

Boyd, I. L., D.J. McCafferty and R. Walker. (1997). Variation in foraging effort by lactating antarctic fur seals: Response to simulated increased foraging costs. Behavioral Ecology and Sociobiology 40:135-144.

Chipman, E. D., N.E. McIntyre., J.D. Ray., M.C. Wallace and C.W Boal (2007) Effects of radiotransmitter necklaces on behaviours of adult male Western Burrowing Owls. Journal of Wildlife Management, 71(5), 1662-1668.

Culik, B and R.P. Wilson. (1991). Swimming energetics and performance of instrumented Adelie enguins (*Pygoscelis adeliae*). Journal of Experimental Biology 158:355-368.

Culik, B.M., R.P. Wilson and R. Bannasch. (1993) Flipper bands on penguins: What is the cost of a life long commitment. Marine Ecology Progress Series, 98, 209 - 214.

Culik, B. M., R. Bannasch., and R.P. Wilson. (1994). External devices on penguins: How important is shape? Marine Biology (Berlin) 118:353-357.

Fackrell, S. (2011) Study of the Added Mass of Cylinders and Spheres. PhD Thesis. University of Windsor.

Fiore, G., E. Anderson., C.S. Garborg *et al.* (2017) From the track to the ocean: Using flow control to improve marine bio-logging tags for cetaceans. PLoS ONE 12(2) URL https://doi.org/10.1371/journal.pone.0170962 [accessed 6th April 2017]

Fish, F., K. Innes and K. Ronald. (1988) Kinematics and estimated thrust production of swimming harp and ringed seals. Journal of Experimental Biology. 137, 157 - 173.

Gaster, M. (1988) Is the dolphin a red herring? Turbulence Management and Relaminarisation International Union of Theoretical and Applied Mechanics (eds Liepmann H.W, Narasimha R.). Springer, Berlin.

Hazekamp, A.H., R. Mayer and N. Osinga. (2009) Flow simulation along a seal: The impact of an external device. *European* Journal of Wildlife Research. 56, 131 - 140.

Hoerner, S. (1965) Fluid Dynamic Drag, published by the author.

Hull, C.L. (1997) The effect of carrying devices on breeding royal penguins. The Condor, 99 (2), 530–534.

Lamb, H. (1932) Hydrodynamics 6th Edition Reprint. Dover Publications (1945). New York, USA.

Langtry, R and F. Menter.(2006) Overview of industrial transition modelling in CFX, Technical Report, ANSYS Inc, USA.

Maresh, J. L., S.E. Simmons., D.E. Crocker., B.I. McDonald., T.M. Williams and D.P. Costa. (2014). Free-swimming northern elephant seals have low field metabolic rates that are sensitive to an increased cost of transport. Journal of Experimental Biology, 217, 1485-1495.

McIntyre, T. (2015) Animal telemetry: Tag effects. Science. 349 (6248), 596 – 597. [doi: 10.1126/science.349.6248.596-b].

McKnight, J. C. (2018) Counting the Cost of Tagging: Quantifying and Reducing the Behavioural and Energetic Impacts of Tags in a Large Marine Vertebrate. Ph.D Thesis, University of St. Andrews.

McMahon, C. R., C.J. Bradshaw and G.C. Hays. (2007). Applying the heat to research techniques for species conservation. Conservation Biology 21:271-273.

McMahon, C. R., N. Collier., J.K. Northfield and F. Glen. (2011). Taking the time to assess the effects of remote sensing and tracking devices on animals. Animal Welfare 20:515-521.

Menter, F.R. (1993) Zonal two-equation k-ω turbulence model for aerodynamic flows. AIAA Paper 93-2906. 24th Fluid Dynamics Conference URL https://ntrs.nasa.gov/archive/nasa/casi.ntrs.nasa.gov/19960044572.pdf [accessed 21st March 2017]

Menter, F.R. (1994) Two-equation eddy-viscosity turbulence models for engineering applications. AIAA Journal. 32 (8), 1598 - 1605.

Menter, F. (2011) Turbulence modelling for engineering flows, Technical Report, ANSYS Inc, USA.

Menter, F., P.E Smirnov., T. Liu., and R. Avancha. (2015) A one equation local correlation-based transition model. Flow, Turbulence and Combustion 95(4): 583-619.

Newman, J, N. (1977) Marine Hydrodynamics. MIT Press. Cambridge, USA.

Pavlov, V.V., R.P. Wilson and K. Lucke. (2007) A new approach to tag design in dolphin telemetry: Computer simulations to minimise deleterious effects. Deep Sea Research Part 2. 54, 404 - 414.

Pavlov, V.V and A.M. Rashad. (2012) A noninvasive dolphin telemetry tag: Computer design and numerical flow simulation. Marine Mammal Science. 28 (1), E16 - E27.

Pope, S. (2000) *Turbulent Flows*, Cambridge University Press, Cambridge, UK.

Rohr, J., M.I. Latz., S. Fallon., J.C. Nauen and E. Hendricks. (1998) Experimental approaches towards interpreting dolphin stimulated bioluminescence. Journal of Experimental Biology. 201, 1447 - 1460.

Ropert-Coudert, Y., R.P. Wilson., K. Yoda and A. Kato. (2007) a. Assessing performance constraints in penguins with externally-attached devices. Marine Ecology-Progress Series 333:281-289.

Ropert-Coudert, Y.,N. Knott., A. Chiaradiac and A. Kato. (2007) b. How do different data logger sizes and attachment positions affect the diving behaviour of little penguins? Deep-Sea Research II, 54, 415–423.

Rosen, D. A. S., D. Gerlinsky., and A.W Trites. (2018) Telemetry tags increase the costs of swimming in northern fur seals, *Callorhinus ursinus*. Marine Mammal Science. 34(2): 385-402.

Saraux, C., C. Le Bohec., J.M. Durant *et al.* (2011) Reliability of flipper-banded penguins as indicators of climate change. Nature, 469, 203-206.

Shorter, K.A., M.M. Murray., M. Johnson., M. Moore and L.E. Howle. (2014) Drag of suction cup tags on swimming animals: Modeling and measurement. Marine Mammal Science. 30 (2), 726 - 746.

Stelle, L.L., R.W. Blake and A.W. Trites. (2000) Hydrodynamic drag in Steller Sea Lions. Journal of Experimental Biology. 203, 1915 - 1923.

Todd Jones, T., K.S. Van Houten., B.L. Bostrom *et al.* (2013) Calculating the ecological impacts of animal-borne instruments on aquatic organisms. Methods in Ecology and Evolution. 4(12), 1178 - 1186.

Vandenabeele, S. P., R.P. Wilson and A. Grogan. (2011). Tags on seabirds: How seriously are instrument-induced behaviours considered? Animal Welfare 20:559-571.

Vogel, S. (1994) Life in Moving Fluids: The Physical Biology of Flow. Princeton University Press. Princeton, USA.

Walker, K.A., A.W. Trites., M. Haulena and D.M. Weary. (2012) A review of the effects of different marking and tagging techniques on marine mammals. Wildlife Research, 39(1), 15 – 30.

Watson, K.P and R. A. Granger. (1998) Hydrodynamic effect of a satellite transmitter on a juvenile Green Turtle. Journal of Experimental Biology. 201, 2497 - 2505.

Williams, T and G. Kooyman. (1985) Swimming performance and hydrodynamic characteristics of harbor seals *Phoca Vitulina*. Physiological Zoology. 58, 576 - 589.

Wilson, R. P., W.S. Grant and D.S. Duffy. (1986) Recording devices on free-ranging marine animals: Does measurement affect foraging performance? Ecology 67:1091-1093.

Wilson, R.P., Y. Ropert-Coudert and A. Kato. (2002) Rush and grab strategies in foraging marine endotherms: The case for haste in penguins. Animal Behaviour, 63 (1), 85 - 95.

Wilson, R.P., J.M. Kreye., K. Lucke and H. Urquhart. (2004) Antennae on transmitters on penguins: Balancing energy budgets on the high wire. Journal of Experimental Biology. 207, 2649 - 2662.

Wilson, R. P and S.P. Vandenabeele. (2012) Technological innovation in archival tags used in seabird research. Marine Ecology Progress Series 451:245-262.

Tables

	Turbulence Model	Boundary Layer Transition Model
Baseline (Method 1)	Shear Stress Transport	γ
Method 2	Shear Stress Transport	None
Method 3	k-ε	None

Table 1: Turbulence and transition modelling approach breakdown

Simulation	Glide Velocity (m/s)	Reynolds Number (Re)
1	0.9 m/s	1.224×10^6
2	1.1 m/s	1.496×10^6
3	1.3m/s	1.768×10^6
4	1.5 m/s	2.040×10^6
5	1.7 m/s	2.312×10^6

Table 2: Fixed velocity simulations; inlet velocities and Reynolds Numbers.

Ambient temperature (^oC)	10
Water density (kg/m^3)	1,027
Water dynamic viscosity (Pa.s)	1.397×10^{-3}

Table 3: Assumed environmental conditions

Inlet	Uniform inlet velocity, value dependent on simulation 1% turbulence intensity
Outlet	Average static pressure (0 Pa)
Tag	No slip smooth wall
Seal	No slip smooth wall
Domain walls	Free slip wall

Table 4: Applied simulation boundary conditions

Simulation No.	Total No. Nodes	No. Nodes Local to Tag	Total Drag (N)	Tag drag (N)
1	3,754,216	896,144	10.75	0.88
2	18,612,508	4,738,948	10.87	0.98
3	20,538,422	6,664,862	10.81	1.07
4	21,773,952	7,900,392	10.82	1.08

Table 5: Mesh dependency study results.

	Baseline Domain	Halved Domain	Quartered Domain
Total Tagged Animal Drag Force (N)	10.81	10.83	10.95

Table 6: Domain dependency study results.

Method	SST-γ (Baseline)	SST Only	k–ε Only
Untagged Animal: Total Drag Force (N)	8.19	9.72	8.87
Untagged Animal: Drag Coefficient ($C_{d\ u}$)	0.0052	0.0062	0.0056
% Force difference to Baseline	-	18.68	8.30

Table 7: Comparison of untagged animal simulated drag forces

Method	SST-γ (Baseline)	SST Only	k–ε Only
Tagged Animal: Total Drag Force (N)	9.52	10.81	9.07
Tagged Animal: Drag Coefficient ($C_{d\ t}$)	0.0060	0.0069	0.0058
% Force increase over untagged case using the same method	16.24	11.21	2.25

Table 8: Comparison of tagged animal simulated drag forces

Figures

Figure 1: Adult female gray seal (*Halichoerus grypus*) with a SMRU GPS phone tag mounted at the base of the skull, on the ventral surface of the neck

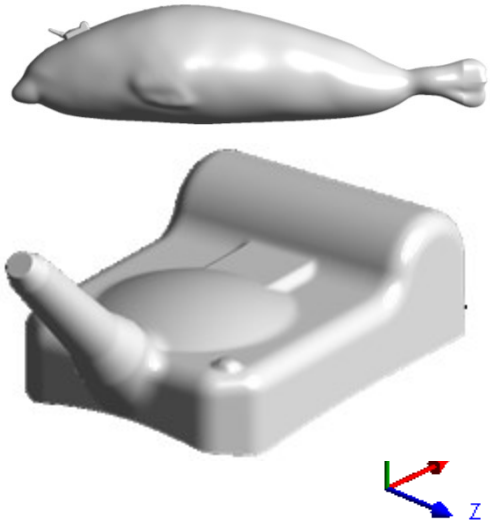

Figure 2: Surface models of tagged seal (top) and tag in isolation (bottom).

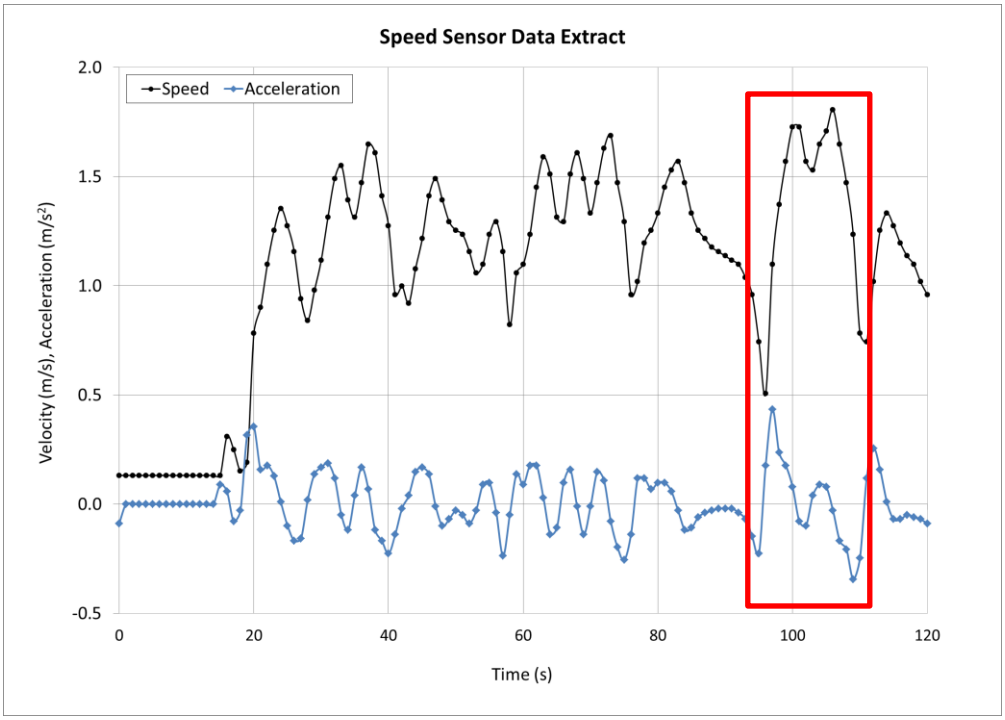

Figure 3: 120 second extract from recorded mean swim speed data.

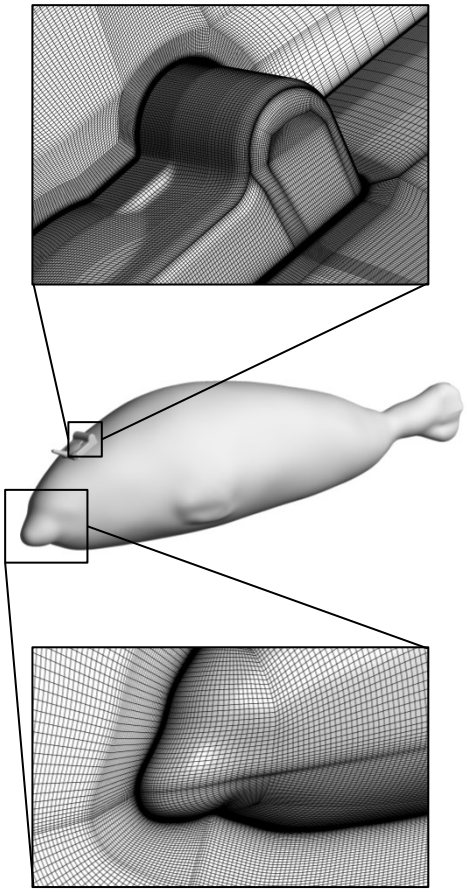

Figure 4: Plots showing the hexahedral mesh applied throughout simulation work. Images show both surface meshes on tag and animal and a cross section of the volume mesh.

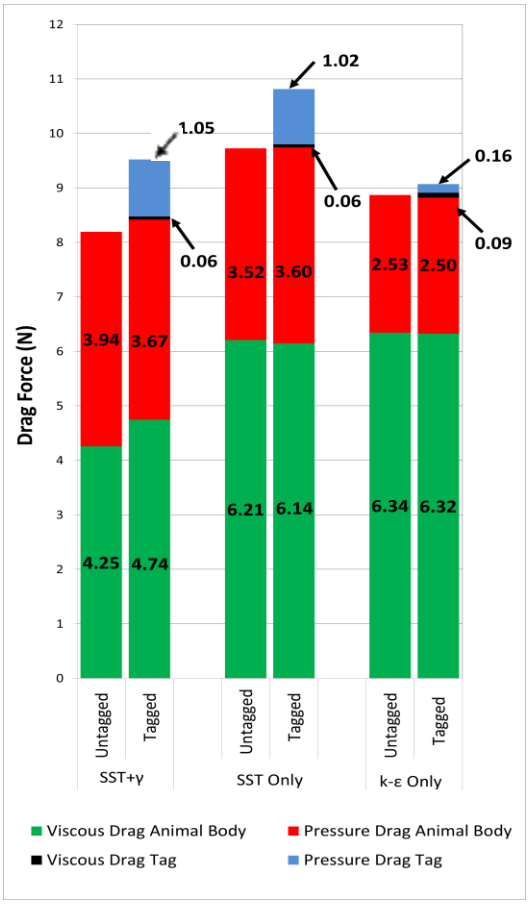

Figure 5: Viscous and pressure drag component breakdown for tagged and untagged animals

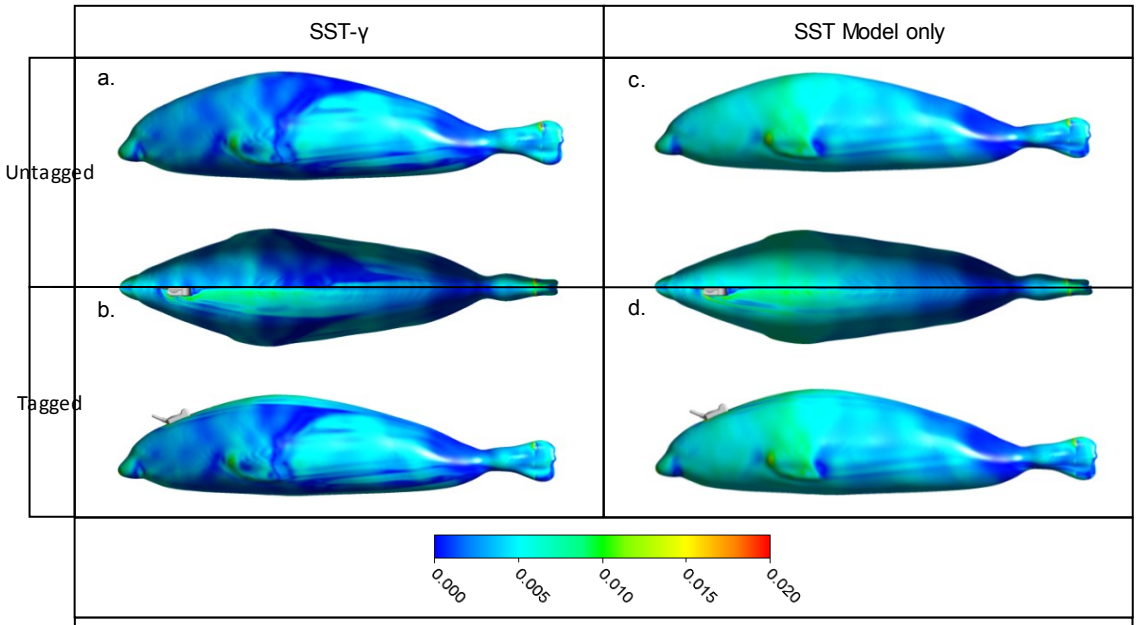

Figure 6: Skin friction coefficient distribution;

(a) SST-γ (Untagged), (b) SST-γ (Tagged), (c) SST only (Untagged), (d) SST only (Tagged)

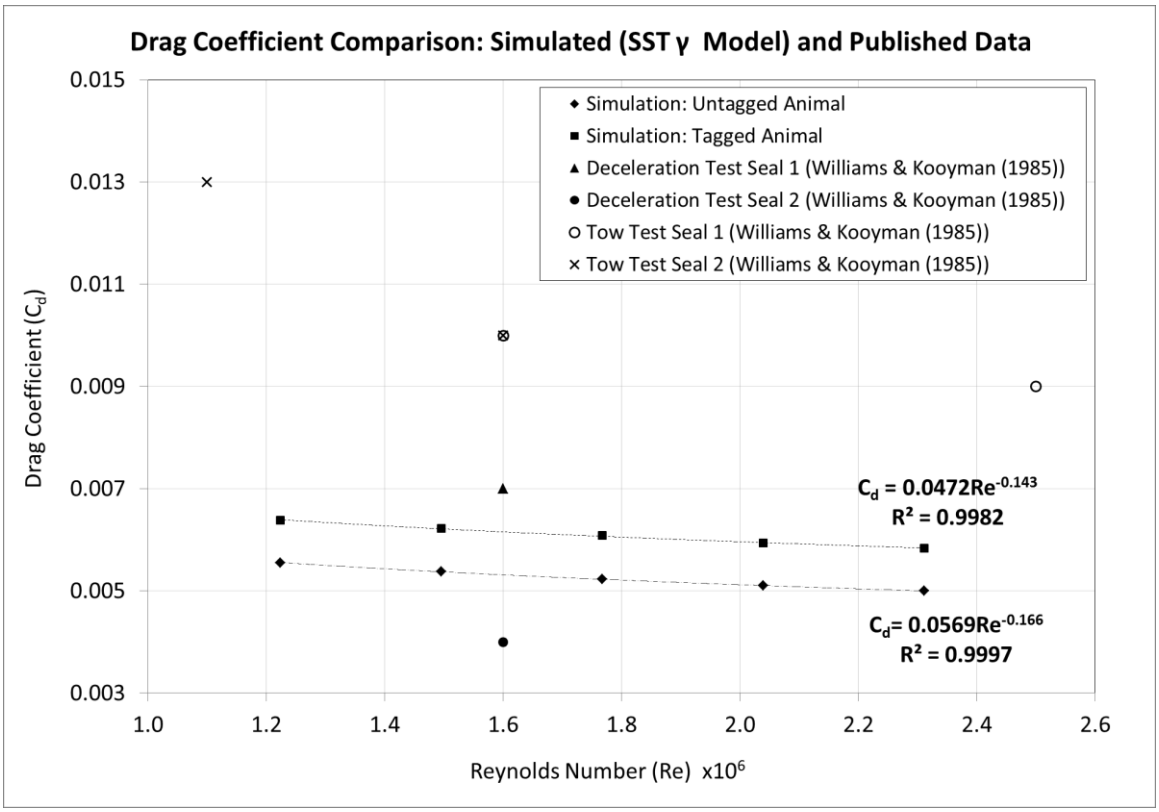

Figure 7: Fixed velocity simulation results showing variation in hydrodynamic drag coefficient (C_d) with Reynolds Number (Re) for both tagged and untagged animal. Simulation results compared with results given by Williams and Kooyman (1985)

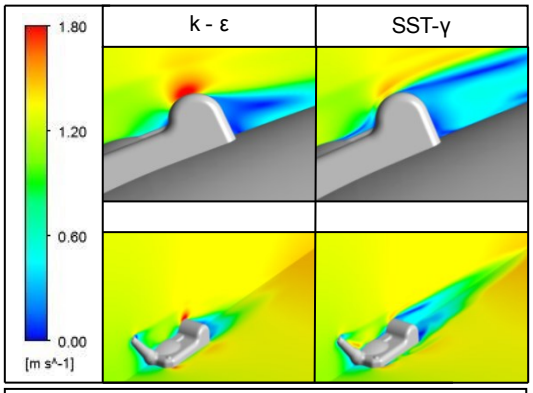

Figure 8: Flow velocity plots comparing predicted tag wake formation for k-ε and SST-γ cases.

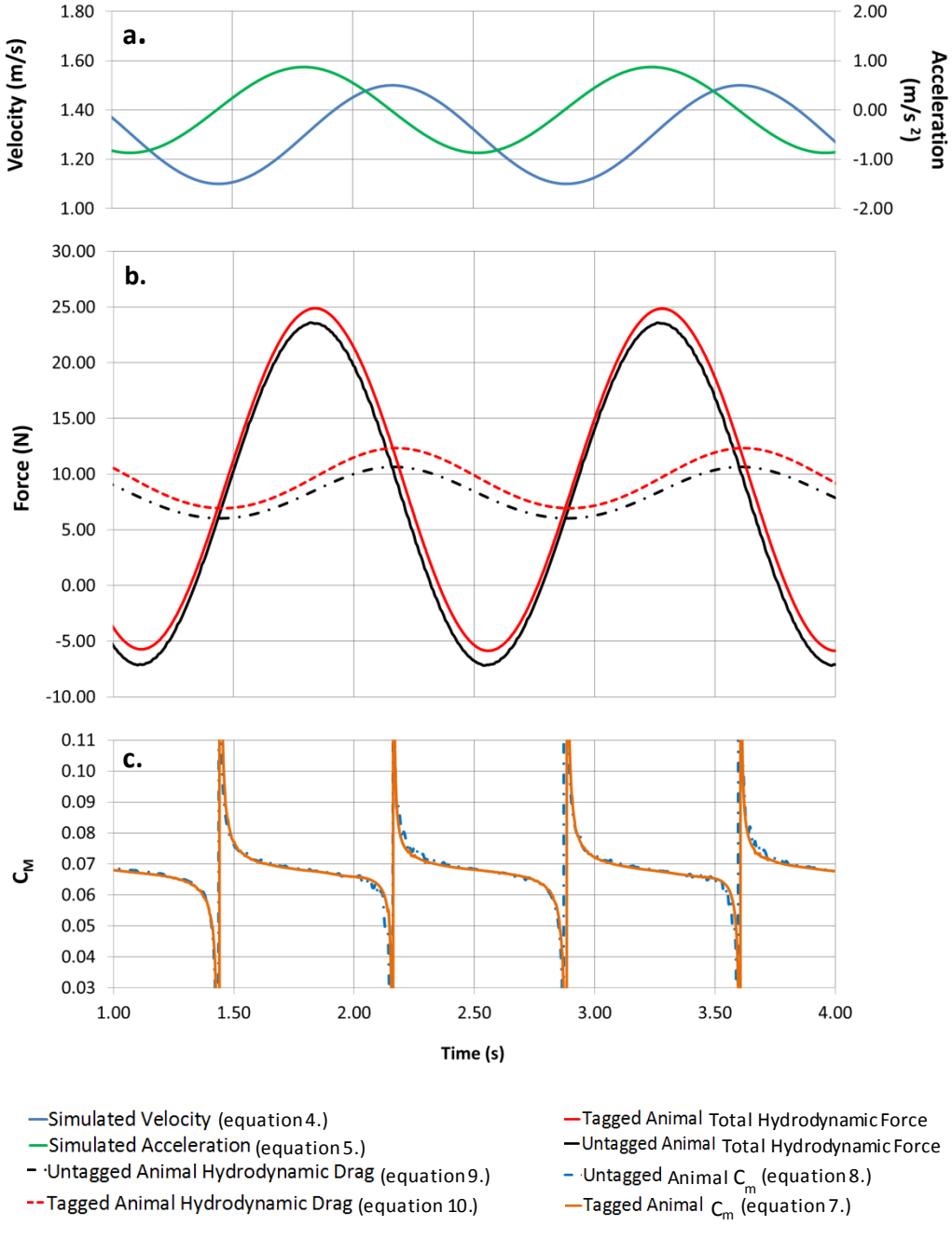

Figure 9: Noninertial reference frame simulation results showing; **a.** Inlet velocity and acceleration variation with time. **b.** Hydrodynamic drag and total hydrodynamic force imposed on both tagged and untagged animal. **c.** C_m for both tagged and untagged animal based on equations 7 and 8 respectively.

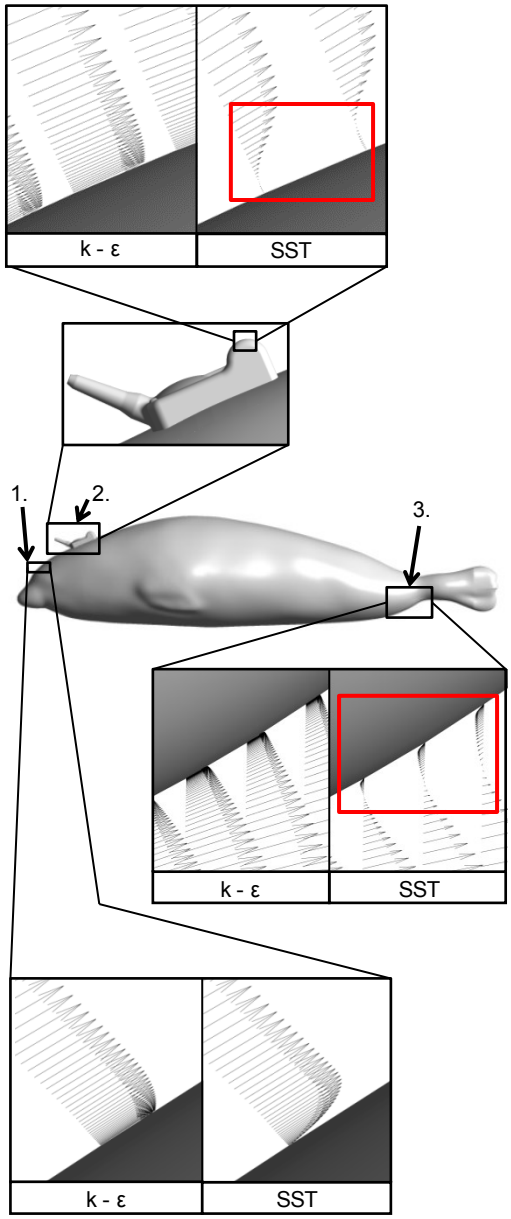

Figure 10: Velocity vector plot comparison between k-ε and SST models at 3 locations. Note that vector length is proportional to flow velocity hence the boundary layer can be visualized.

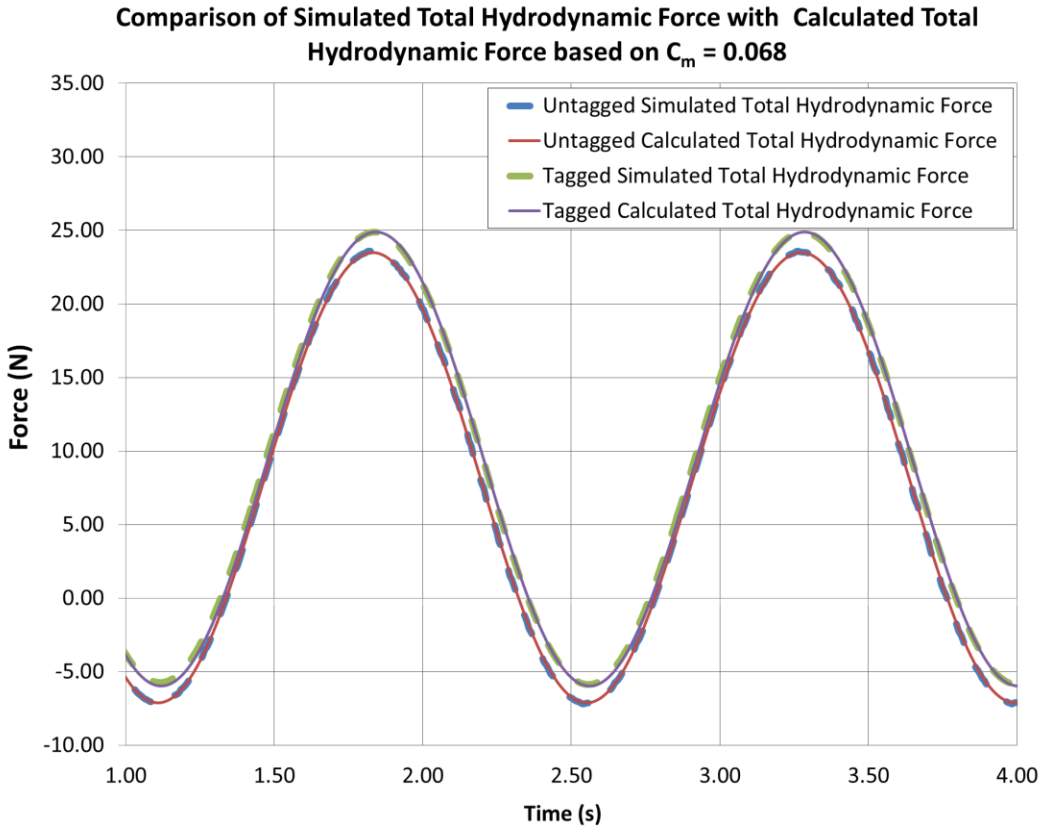

Figure 11: Comparison of total hydrodynamic force as predicted by simulation and as predicted from calculation (Calculation based on C_m of 0.068 at and C_d from equations 9 and 10 for the untagged and tagged animal, respectively).

Supplementary Material Part A – Hydrodynamic Theory

This supplementary material is provided as a point of reference for those interested in the CFD work presented in the main paper but not necessarily familiar with the key underlying physics of flow around the bodies typical of many highly streamlined marine mammals. More detailed consideration of these key physics from a purely fluid mechanical perspective can be found in Hoerner (1965) and Marchaj (1988) while Vogel (1994) gives a detailed consideration of the relevant principles in the biological context. A summary of the key information is given here, in order to illustrate the key capabilities that any CFD approach must possess.

Nomenclature

a = Acceleration (m/s^2)

C_d = Drag coefficient (based on wetted area of animal)

C_m = Added mass coefficient

F = Total resistive force (N)

L = Characteristic length (in this case the length of the body) used to calculate Re (m)

m = Animal mass (kg)

Re = Reynolds number based on animal length

S = Animal wetted area (m^2)

u = Velocity (m/s)

V = Animal displaced volume (m^3)

ρ = Density of fluid (kg/m^3)

μ = Dynamic viscosity (Pa.s)

Forces at a Fixed Velocity – Hydrodynamic Drag

Figures 1a-c show an idealized form of a typical marine mammal. In negotiating a path around the body, the speed of the fluid varies[6] due to its shape, giving rise to a variation in pressure around the body. Part of the drag force experienced by the body is due to this pressure variation. The remainder of the drag force is due to the frictional effect of the fluid passing the body. Viscosity causes the fluid particles in proximity to the body to be slowed down by the presence of the body's surface, causing a tangential *viscous* drag force. The region over which this occurs is known as the boundary layer. Initially, flow in the boundary layer is "laminar"; fluid particles flow parallel to the surface in an ordered fashion, typically over the anterior portion of the body. Due to factors such as local flow conditions or surface roughness, this ordered flow becomes unstable and decays to a fully turbulent state in a process known as boundary layer transition. As illustrated in Figure 1b, the boundary layer thickens rapidly, develops fluctuating, chaotic eddies and the *viscous drag increases significantly compared to its laminar counterpart*. The sum of the *viscous* and *pressure* drag components is the *hydrodynamic drag*.[7]

The proportion of the body experiencing laminar flow relative to turbulent flow affects the amount of viscous drag experienced, whilst pressure drag is highly sensitive to the point at which the boundary layer *separates* away from the body, forming a turbulent wake. This wake is at a pressure significantly lower than upstream of the body and this pressure difference results in a drag force; thus, a body that inhibits separation minimizes pressure drag. Marine mammals are shaped to avoid or delay separation as per Figure 1a. However, abrupt dimension changes and protrusions typical of 'bluff' bodied tags can induce highly separated flows, large wakes and high pressure drag.

On smoothly curved bodies, the relative importance of pressure and viscous drag forces is governed by how the boundary layer responds to the pressure variation induced in the surrounding fluid. Comparison of idealized streamlined bodies (Figs. 1a-c) with more bluff bodies (Figs. 2a-c) shows how body shape influences these forces. In Figure 1a, fluid experiences a "favorable pressure gradient" between points 1 and 2; fluid accelerates up the anterior face of the body and its static pressure reduces until the maximum velocity (minimum pressure) occurs at the widest point of the body. Between points 2 and 3, it experiences an "adverse pressure gradient"; flow decelerates along the posterior face with static pressure increasing back to that of the undisturbed fluid at the rearmost point. The rate of pressure increase depends on the steepness of the posterior taper.

---

[6] To describe hydrodynamic drag, a common convention is followed, in which the body is considered stationary with oncoming fluid moving at a velocity equivalent to swim speed.

[7] Note that this definition of hydrodynamic drag assumes the body is fully submerged and far from the free surface. In cases where the submergence depth is shallower than approximately one body length, there will be an increase in pressure drag associated with the energy required to distort the free surface, commonly known as wave drag.

Boundary layer stability is affected by this pressure variation. The favorable pressure gradient on the anterior face stabilizes the boundary layer, while the adverse pressure gradient over the posterior face causes instability, and hence transition from laminar to turbulent flow. In many cases, boundary layer transition on a *smooth* body occurs at the widest point (Hoerner 1965).

Steep posterior tapering can bring fluid to a halt (causing boundary layer separation well ahead of the posterior tip) due to the retarding effect of the pressure gradient. The shorter, more steeply tapering body of Figure 2c creates a *steeper* adverse pressure gradient than that of Figure 1c; separation occurs closer to the nose, creating a larger wake size and much higher pressure drag. Indeed, pressure drag will dominate in highly separated bluff cases while viscous drag is likely to be larger on bodies with little or no separation.

Turbulent flows can have their benefits. In comparison to its laminar counterpart, a turbulent boundary layer carries more fluid momentum, so can overcome an adverse pressure gradient for longer, retarding separation. A useful analogy is the flow over a golf ball; the dimples force boundary layer transition further forward in comparison to a smooth ball. The increased viscous drag is more than offset by a reduction in pressure drag from the delayed separation, and results in total drag being reduced.

The Reynolds Number (Re), a nondimensional measure of the relationship between viscous and inertial effects within the boundary layer indicates whether significant portions of laminar flow are likely (equation 1).

$$Re = \frac{\rho u L}{\mu} \qquad (1.)$$

According to data presented by Hoerner (1965), in terms of an *idealized smooth axisymmetric streamlined body*, below Re of approximately 1×10^5 the boundary layer may be predominantly laminar. The proportion of turbulent boundary layer increases with Re until, at a value between approximately 5×10^6 and 1×10^7, it is likely to be almost entirely turbulent It is important to note, however, that boundary layer transition may occur much closer to the nose of a body that possesses the imperfections present on a real animal (*i.e.*, Fur, vibrissae etc.).

Reliable boundary layer transition prediction is therefore essential when predicting the drag of the animal body and the net drag increase imposed by an ABDL (or ''tag''). An ABDL constitutes a major surface imperfection, so if located far forward enough to be in a naturally laminar portion of the boundary layer it will certainly force transition; the total drag increase will be the hydrodynamic drag of the tag *plus* the associated additional viscous drag due to the increased proportion of turbulent boundary layer over the animal skin/fur/feather/carapace. Neglecting this additional viscous drag by assuming a fully turbulent boundary layer would *under-predict* the impact of a tag. For CFD methods to be reliable, they must reliably predict viscous drag and, by extension, boundary layer transition in order to estimate the drag imposed on

the streamlined animal body. They must also provide reasonable pressure drag, and therefore boundary layer separation prediction in order to model the drag of the relatively bluff bodied tag.

Forces Due to Acceleration – Acceleration Reaction Force (based on the discussion given by Vogel 1994)

The preceding discussion has considered the force resisting animal motion only under steady conditions, those in which velocity does not vary with time but does vary from point to point, for example as the fluid passes around the moving body. In reality, an animal is likely to be accelerating in one or more degrees of freedom almost all the time, whether this be during normal swimming (the acceleration and deceleration arising as a consequence of a 'kick and glide' swim pattern), during direction changes, prey pursuit episodes and also during predator evasion.

Consequentially, the 'steady flow' assumption (*i.e.,* that hydrodynamic drag is the only force resisting motion) represents a significant over-simplification of reality. Indeed during periods of acceleration, hydrodynamic drag constitutes only one component of the total force that resists motion.

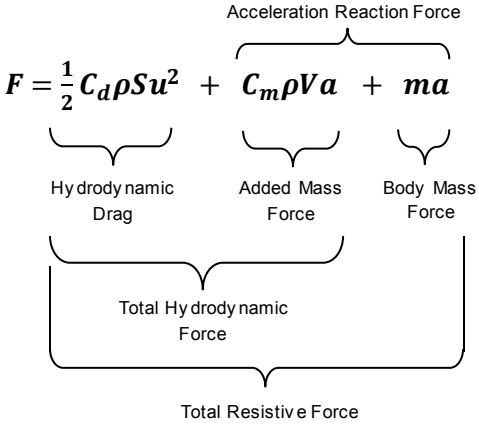

(2.)

Equation 2 (Vogel 1994) shows that the total resistive force acting on an accelerating animal (or alternatively the total thrust an animal must generate at any given time) is actually the sum of 3 components, the velocity dependent hydrodynamic drag already discussed and two additional acceleration dependent forces; the *added mass force* and the *body mass force* – collectively termed the *acceleration reaction force*.

The body mass force is simply the thrust an animal must generate to accelerate its own body mass forwards while the added mass force arises because, in order for the animal to accelerate forwards, a volume of fluid has to be moved, or accelerated backwards. This is often considered as an extra mass of fluid, in addition to the mass of the body, which is accelerated with the animal, hence the term 'added mass'. The actual amount of fluid assumed to be accelerated with the

animal is determined by the added mass coefficient (C_m) which defines the mass to be added as a proportion of the displaced mass of the body. It is important to note that a body will exhibit a range of C_m values with the actual value dependent on the direction of acceleration. Consequentially, a given C_m must be stated along with the direction of body motion to which it relates.

For some simple 2D and 3D cases (for example circular cylinders, spheres and spheroids) analytical solutions for C_m, based on potential flow theory, are available (see Lamb 1932 and Newman 1977). It should be noted that these solutions, by definition, neglect the effect of boundary layers and wakes, flow features present on any real body. In reality such features are likely to have the effect of artificially increasing the effective volume of the body. It is therefore reasonable to suggest that for highly streamlined bodies with comparatively small wakes, the error in C_m induced by the assumption of potential flow may be small since the effective volume is not greatly different from the actual volume. Conversely in the case of a more bluff body with a large wake (and therefore a much larger effective volume in comparison to the actual volume) this error may be much larger. Care must therefore be taken when applying C_m values based on potential flow theory.

In order to make a realistic estimate of tag impact, it is not enough to consider only the effect of its presence on the hydrodynamic drag component of the total resistive force. Rather, some effort should be made to predict its impact, if any, on the added mass component of the acceleration reaction force as well.

References

Hoerner, S. (1965) Fluid Dynamic Drag, published by the author.

Lamb, H. (1932) Hydrodynamics *6th Edition Reprint.* Dover Publications (1945). New York, USA.

Marchaj, C.A. (1988) Aero - Hydrodynamics of Sailing, Adlard - Coles Nautical, London, UK.

Newman, J, N. (1977) Marine Hydrodynamics. MIT Press. Cambridge, USA.

Vogel, S. (1994) Life in Moving Fluids: The Physical Biology of Flow. Princeton University Press. Princeton, USA

Figures

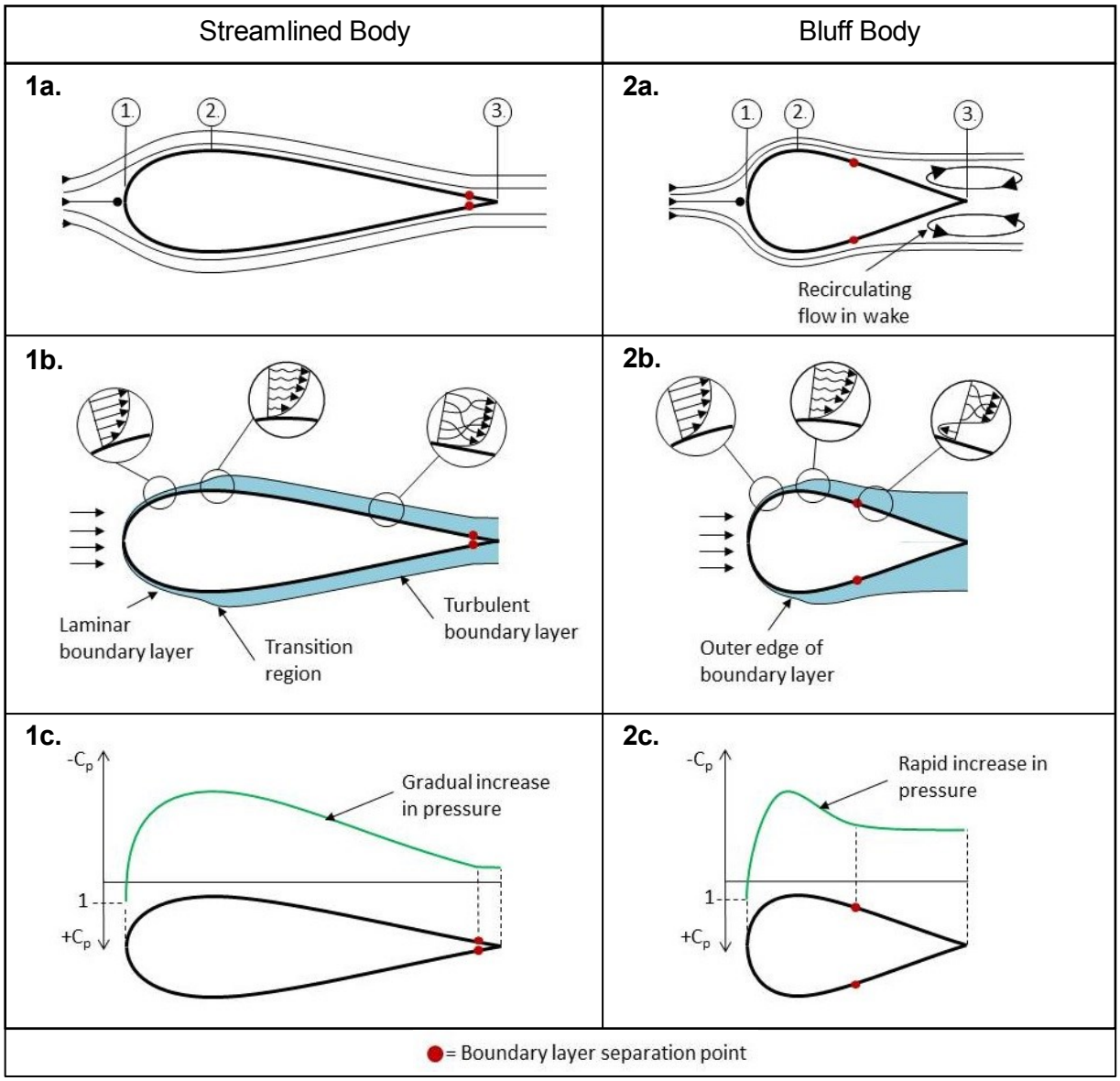

Figures 1a to 2c: Comparison of flow around an idealised, smooth streamlined body (Figures 1a – 1c) and an idealised, smooth bluff (separating) body (Figures 2a – 2c) showing:

1a & 2a: Flow streamlines around body indicating boundary layer separation points and associated wake size.

1b & 2b: Boundary layer growth and transition to turbulence. Note: Boundary layer thickness exaggerated for clarity.

1c & 2c: Pressure coefficient, C_p (a normalised measure of pressure variation) around the body surface induced by fluid velocity changes. Note: Negative C_p is conventionally plotted upwards, thus a downward slope indicates increasing pressure.

Supplementary Material Part B

Validation of a Simulation Methodology for Predicting the Added Mass Coefficient of an Accelerating Body

Nomenclature

$\boldsymbol{a}$ = Acceleration (m/s^2)

$\boldsymbol{A}$ = Amplitude of sinusoidal velocity oscillation (m/s)

$\boldsymbol{C_d}$ = *Drag Coefficient*

$\boldsymbol{C_{m\_th}}$ = *Theoretical added mass coefficient based on potential flow theory*

$\boldsymbol{C_{m\_sim}}$ = *Added mass coefficient based on simulation*

$\boldsymbol{f}$ = Frequency of sinusoidal velocity oscillation (Hz)

$\boldsymbol{F}$ = Total resistive force (N)

$\boldsymbol{L}$ = Length of spheroid (L)

$\boldsymbol{V}$ = Total volume of displaced water (m^3)

$\boldsymbol{Re}$ = Reynolds Number based on spheroid major axis length L

$\boldsymbol{g_x}$ = Gravitational acceleration vector in the x-direction (m/s^2)

$\boldsymbol{S}$ = Spheroid wetted area (m^2)

$\boldsymbol{t}$ = Time (seconds)

$\boldsymbol{u_{in}}$ = Instantaneous inlet velocity (m/s)

$\boldsymbol{u_{mean}}$ = Mean velocity (m/s)

$\boldsymbol{u}$ = Velocity in x-direction (m/s)

$\boldsymbol{v}$ = Velocity in y-direction (m/s)

$\boldsymbol{w}$ = Velocity in z-direction (m/s)

$\boldsymbol{x}$ = Cartesian coordinate axis aligned with the longitudinal axis of spheroid (m)

$\boldsymbol{y}$ = Cartesian coordinate axis perpendicular to longitudinal axis of spheroid in vertical direction (m)

z = Cartesian coordinate axis perpendicular to longitudinal axis of spheroid in horizontal direction (m)

φ = Phase (Radians) Used to define starting velocity during sinusoidal velocity simulations.

ρ = Density of water (kg/m^3)

Introduction

As shown at equation 1, the total resistive force acting on an accelerating body is the sum of three components; the hydrodynamic drag, the added mass force and the body mass force. The body mass force is easily computed from Newton's 2nd Law and the variation of hydrodynamic drag with velocity (and therefore Re) can be predicted through a series of fixed velocity CFD simulations. A considerably more complex simulation methodology is required in order to predict the added mass coefficient (C_m) and therefore the added mass force.

$$\underbrace{F = \underbrace{\frac{1}{2}C_d\rho S u^2}_{\text{Hydrodynamic Drag}} + \overbrace{\underbrace{C_m\rho V a}_{\text{Added Mass Force}}}^{\text{Acceleration Reaction Force}} + \underbrace{ma}_{\text{Body Mass Force}}}_{\text{Total Resistive Force}} \qquad (1.)$$

Total Hydrodynamic Force

This supplementary material details the simulation work conducted in order to develop and validate a means by which the effects of this force can be captured. The necessary switch to a noninertial frame of reference is implemented via the inclusion of an additional body force (per unit volume of fluid), acting in the direction of flow, thereby capturing the additional inertial forces arising during body acceleration / deceleration. The method developed does not require the use of moving or deforming computational meshes.

Reference Geometry and Published C_m

The developed methodology is used to predict the *total hydrodynamic force* acting on a prolate spheroid with a fineness ratio of 5 (side and front views of the spheroid are shown at figure 1 while dimensions of the major and minor axis are given at table 1 along with additional required geometric information). The prolate spheroid was selected as a suitable reference case as it represents an idealised form of the highly streamlined bodies typical of many marine mammals; in

addition there is a readily available, widely published analytical solution for C_m. Table 1 shows C_m (as calculated from potential flow theory) given by Newman (1977).

Methodology

Prediction of Hydrodynamic Drag Component of Total Hydrodynamic Force

In order to predict the variation in hydrodynamic drag with inlet flow velocity (and therefore with Re), a set of 5 fixed velocity simulations were conducted as per table 2. Results of the simulations conducted allow the variation observed to be expressed in an equation of the form given at equation 2, thereby allowing C_d (and therefore hydrodynamic drag) to be predicted for any instantaneous flow velocity.

$$C_d = xRe^{-y} \tag{2.}$$

Prediction of Total Hydrodynamic Force Based on Calculation (Using C_{m_th})

Based on the simulated C_d variation and C_{m_th} given by Newman (1977) it is possible to calculate, for any given temporal velocity profile, the expected total hydrodynamic force acting on the spheroid as long as the instantaneous acceleration of the flow is also known.

A sinusoidal variation in inlet velocity offers a convenient means by which to perform these calculations because there is an analytical solution which can be used to determine acceleration at any point in the velocity cycle. Such an approach also offers a means by which to check simulation solution stability when using simulations to predict the total hydrodynamic force (detailed in the following section); if there is negligible difference in the force predicted at comparable flow speeds across multiple sinusoidal oscillations, the simulation is converged and stable.

Equations 3 and 4 show the expressions used to calculate the expected hydrodynamic drag and added mass force for use in equation 1, thereby predicting the total hydrodynamic force based on potential flow theory.

$$u = u_{in} = Asin(2\pi ft + \varphi) + u_{mean} \tag{3.}$$

$$a = \frac{du_{in}}{dt} = 2\pi f\ [Acos(2\pi ft + \varphi)] \tag{4.}$$

The maximum and minimum values of u_{in} applied in the calculations were 3.57 m/s and 1.785 m/s respectively and velocity varied sinusoidally about an u_{mean} of 2.677 m/s yielding amplitude A of 0.893 m/s. A phase φ of 4.172 radians was selected in order to ensure calculations started from the minimum velocity occurring across the cycle and a frequency f of 7.783 Hz was selected in order to ensure acceleration was high enough that the added mass force constitutes a significant proportion of the total hydrodynamic force calculated at peak acceleration.

Prediction of Total Hydrodynamic Force Based on Simulation

In order to predict the total hydrodynamic force by simulation it is necessary to shift from the inertial reference frame to a noninertial reference frame, thus fully capturing the added mass force. While this could be achieved by modelling the spheroid as an immersed solid which accelerates through a body of stationary fluid, this approach can be highly computationally expensive (requiring techniques such as overset mesh or moving/sliding mesh) and can also limit the accuracy of near-wall flow predictions. Any modelling approach which reduces the reliability of boundary layer behaviour prediction is not suitable in cases where accurate hydrodynamic drag and therefore hydrodynamic force prediction is required, therefore a different approach is required.

It is, however, possible to achieve the required switch of reference frames while keeping the body still and accelerating the fluid by including an additional body force per unit volume S_x within the Navier-Stokes conservation of momentum equation in the direction of flow (equation 5.). This body force is applied to the entire volume of fluid contained within the simulation domain and therefore implements the inertial effects present in the real case.

$$\rho\left(\frac{\partial u}{\partial t}+u\frac{\partial u}{\partial x}+v\frac{\partial u}{\partial y}+w\frac{\partial u}{\partial z}\right)=-\frac{\partial p}{\partial x}+\mu\left(\frac{\partial^2 u}{\partial x^2}+\frac{\partial^2 u}{\partial y^2}+\frac{\partial^2 u}{\partial z^2}\right)+\rho g_x+S_x \quad (5.)$$

Where:

$$S_x=\rho a \quad (6.)$$

Equation 3 is used to define the simulation inlet velocity while equation 4 is used to determine the applied body force given by equation 6. The maximum and minimum inlet velocity, f and φ values used in order to calculate the predicted total hydrodynamic force (and detailed in the previous section) have been applied in simulation work to ensure the total hydrodynamic force predicted by simulation can be directly compared to that predicted by calculation. Equation 7 can then be used to determine C_{m_sim} for comparison with C_{m_th}.

$$C_{m\_sim}=\frac{F-(\frac{1}{2}C_d\rho S u^2)}{\rho V a} \quad (7.)$$

Note that F in equation 7 does *not* include the body mass force term (present in equation 1) as in all simulation work the spheroid is a massless void. In this context F is therefore equal to the total hydrodynamic force only.

Geometry Generation and Meshing

The spheroid geometry was generated using Solidworks 2014 CAD software. Fully hexahedral meshes developed using ANSYS ICEM CFD V18 were used throughout simulation work.

Modelling Assumptions

The spheroid is assumed to be rigid, hydrodynamically smooth and perfectly aligned with the incident flow.

Flow around the spheroid is assumed to be symmetrical about the x-y plane as shown at figure 1. As such, only half of the body is modelled in order to reduce computational expense with a symmetry boundary condition applied on the x-y plane. All results shown therefore relate to the half spheroid.

Boundary Conditions, Setup and Solver

Tables 3 and 4 detail the fluid properties and boundary conditions applied respectively.

The computational domain extended 5 body lengths upstream, above, below and along the side of the spheroid and 15 body lengths downstream. ANSYS CFX V18 was used throughout to solve the discretized RANS equations. All simulations applied the SST turbulence model. All simulations conducted were fully transient and an adaptive time-stepping scheme was applied with parameters set to achieve a residual convergence target of 1×10^{-5} within 5 coefficient loops.

All simulations were conducted on a desktop PC equipped with an Intel Core i7 – 3820 processor with 64GB RAM. Fixed velocity simulations took approximately 12 hours to solve while the single simulation run using the sinusoidally varying inlet velocity took approximately 24 hours to yield around 1 second of simulated time.

Results

Hydrodynamic Drag Variation with Inlet Velocity (Fixed Velocity Simulations)

Figure 2 shows the variation in Cd with Re as predicted by the 5 fixed velocity simulations detailed at table 2. C_d decreases from just over 0.00662 at $Re = 2 \times 10^5$ to around 0.00576 at $Re = 4 \times 10^5$, a decrease of around 13%. Equation 8 shows the resulting expression which can be used to predict C_d and therefore the hydrodynamic drag component of the total hydrodynamic force for any velocity within the simulated range.

$$C_d = 0.0764 Re^{-0.2} \tag{8.}$$

Calculated & Simulated Total Hydrodynamic Force

Figures 3a. to 3c. detail and compare total hydrodynamic forces predicted both by calculation and by simulation. Results are given for a 0.3 s time period (just over 2 complete sinusoidal velocity cycles) and show:

- Figure 3a: Simulated velocity and acceleration profiles as detailed by equations 3 and 4.

- Figure 3b: The variation in time of the hydrodynamic drag force (as predicted by equation 8), the calculated total hydrodynamic force (based on C_{m_th}) and the simulated total hydrodynamic force modelled *via* the inclusion of the body force defined at equations 4 and 6.)
- Figure 3c: The variation in C_{m_sim} with time as calculated from equation 7.

Some key observations are:

- The selected acceleration parameters have resulted in a significant and measurable added mass force. At peak acceleration, the hydrodynamic drag constitutes 65% of the total hydrodynamic force predicted by both calculation and simulation meaning the remaining 35% is due to the added mass force.
- There is very close agreement between calculated and simulated total hydrodynamic forces with a measurable difference only evident when the force approaches its minimum and maximum values. Simulation appears to over-predict total hydrodynamic force at the maximum value by around 2% and under-predict total hydrodynamic force at the minimum value by around 6.4% over respective calculated values.
- C_{m_sim} varies across the velocity cycle because as acceleration tends to zero in equation 7, C_{m_sim} tends to infinity.
- C_{m_sim} appears to vary very slightly between peak acceleration and peak deceleration with values of 0.063 and 0.065 respectively, yielding a mean of approximately 0.064, an increase of around 6.66% over the C_{m_th} value of 0.06.

Discussion

Reference to Figure 3b shows that the total hydrodynamic forces predicted by calculation and simulation agree closely, indicating that the method developed and presented here is a valid and accurate means by which to capture the added mass force.

C_{m_sim} appears to vary slightly between peak acceleration and peak deceleration but yields an approximate mean (C_{m_mean}) of 0.064. Figure 4 compares the total hydrodynamic force as predicted by calculation (where C_{m_th} is applied), by simulation and also by calculation when C_{m_mean} is applied. Close agreement between the original simulated force and the calculated force based on C_{m_mean} indicates that the error induced by the difference between C_m at peak acceleration and deceleration is likely to be small and the assumption of a single C_m equal to C_{m_mean} is reasonable in this case.

C_{m_mean} is approximately 6.66% greater than C_{m_th} (based on potential flow theory). This small over-prediction in C_m is expected and can probably be attributed to the larger *effective* volume of the simulated spheroid over the potential flow case due to the presence of both a boundary layer and a wake, as indicated at figure 5.

Conclusion

Work presented in this supplementary material details the methodology developed in order to predict the added mass component of the total hydrodynamic force acting on a body accelerating through a comparatively dense fluid. The method developed holds the body stationary and accelerates flow thereby eliminating the complications that arise when modelling immersed solids accelerating through stationary fluid (where high quality boundary layer resolution is difficult or indeed impossible to achieve). It is based on the application of a sinusoidally varying inlet velocity and the implementation of a user defined source term that adds a body force per unit volume to the conservation of momentum equation in the direction of motion. Simulation results presented show that this method predicts a total hydrodynamic force that agrees closely with that calculated from C_m based on potential flow theory. Having determined C_m and an expression for C_d as a function of Re, the total hydrodynamic force may now be calculated for any instantaneous velocity and acceleration, irrespective of whether they are varying sinusoidally or not.

References

Newman, J, N. (1977) *Marine Hydrodynamics*. MIT Press. Cambridge, USA.

Tables

Major axis length L. (m)	0.1
Minor axis length b. (m)	0.02
Spheroid wetted area (m^2)	5.019×10^{-3}
Spheroid displaced volume (m^3)	2.09×10^{-5}
Published C_m (from Newman 1977)	0.06

Table 1: Prolate spheroid geometric data

Simulation Number	Inlet Velocity (m/s)	Re
1	1.785	2.0×10^5
2	2.231	2.5×10^5
3	2.677	3.0×10^5
4	3.124	3.5×10^5
5	3.570	4.0×10^5

Table 2: Details of fixed velocity simulations conducted in order to determine hydrodynamic drag variation with velocity and Re.

Ambient temperature (^oC)	25
Water density (kg/m^3)	997
Water dynamic viscosity (Pa.s)	8.9×10^{-4}

Table 3: Assumed fluid properties and conditions

Inlet	Uniform inlet velocity, value dependent on simulation 1% turbulence intensity
Outlet	Average static pressure (0 Pa)
Spheroid	No slip smooth wall
x-y plane intersecting spheroid	Symmetry
Domain walls	Free slip wall

Table 4: Applied boundary conditions

Figures

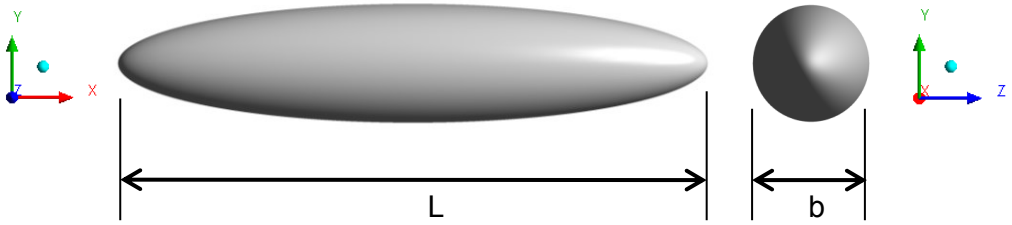

Figure 1: Prolate spheroid and applied coordinate axis

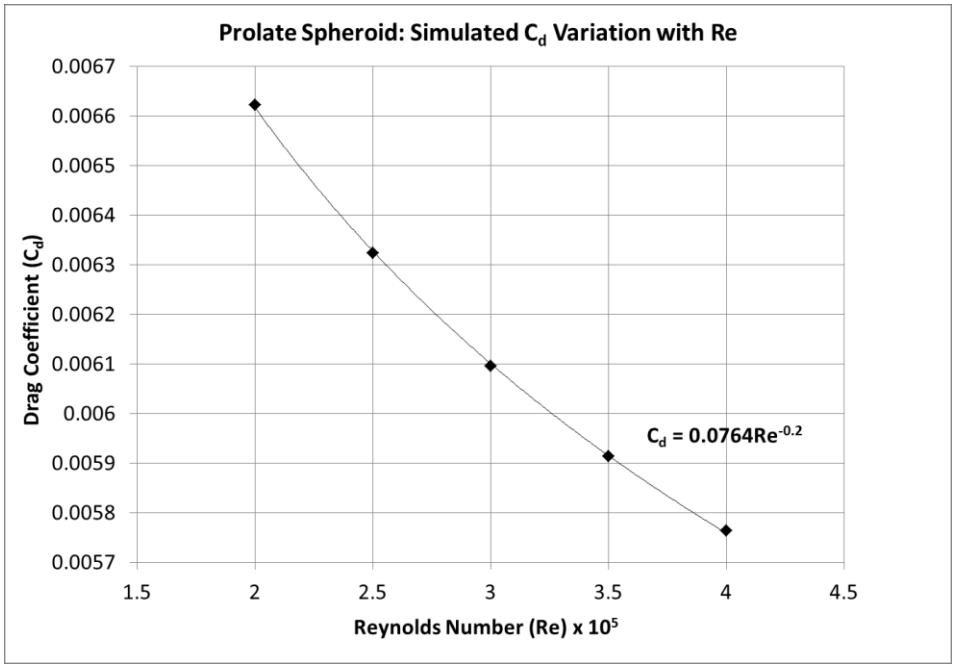

Figure 2: Graph showing variation of C_d with Re based on fixed velocity simulations

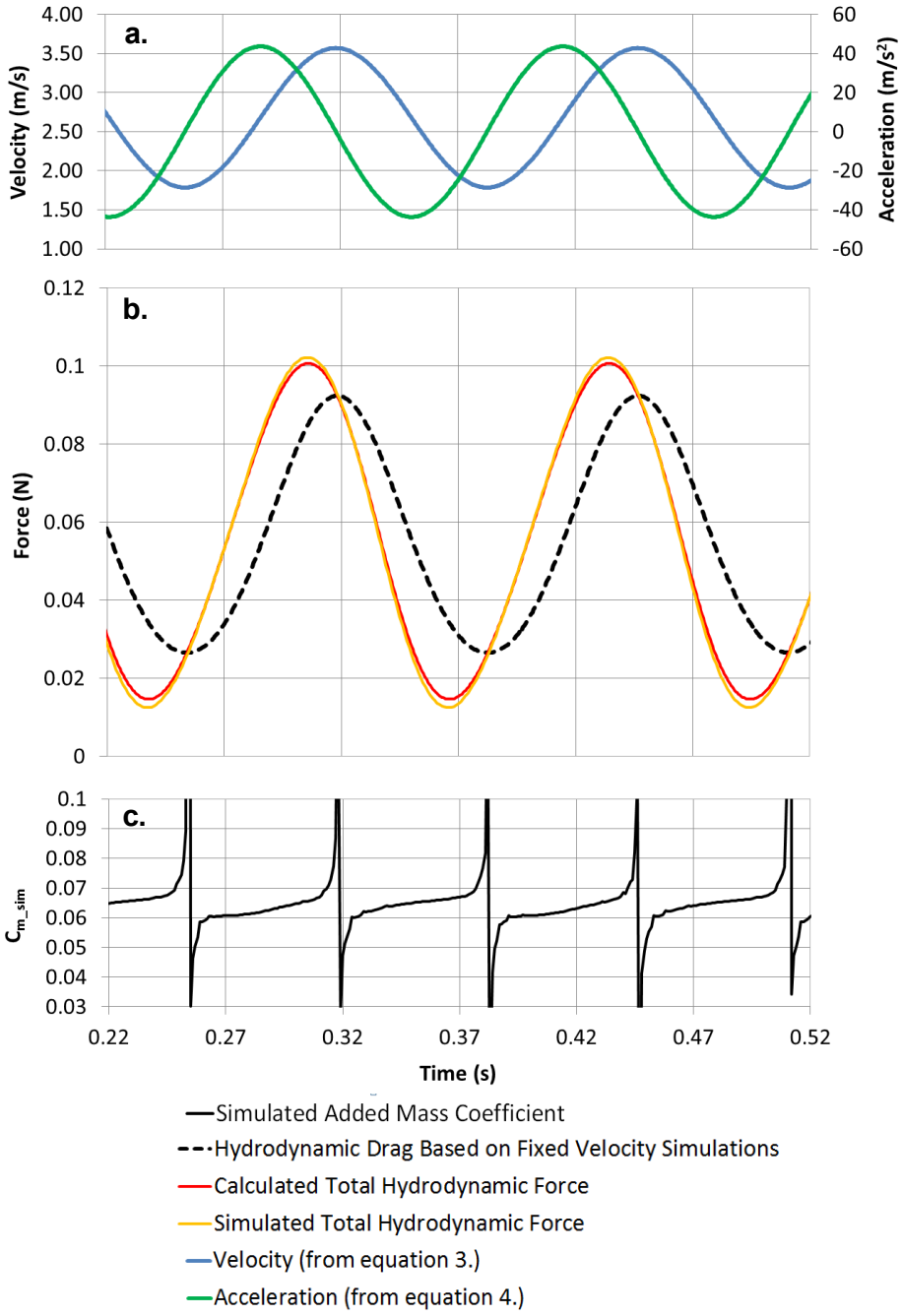

Figures 3a. to 3c. show ing:

Figure 3a: Applied velocity and acceleration. ***Figure 3b***: Predicted hydrodynamic drag force and total hydrodynamic force predicted by calculation and simulation. ***Figure 3c:*** Added mass coefficient as predicted by simulation (C_{m_sim})

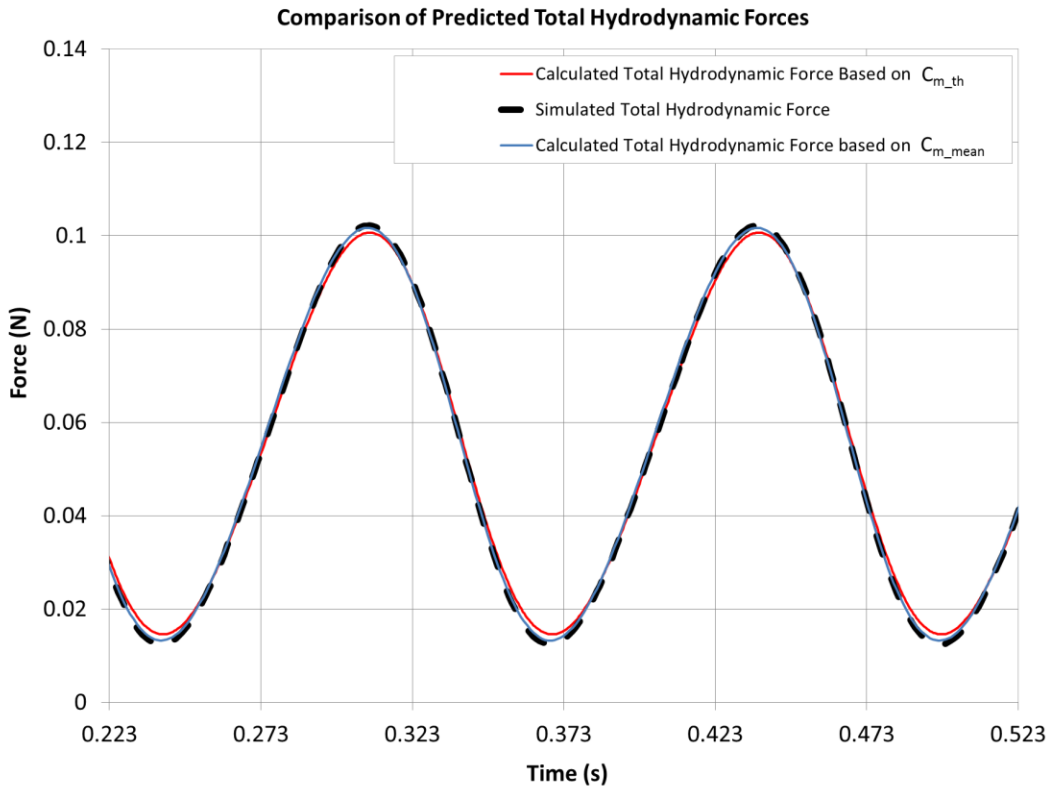

Figure 4: Comparison of total hydrodynamic force as predicted by simulation, calculation based on potential flow theory and calculation based on C_{m_mean}.

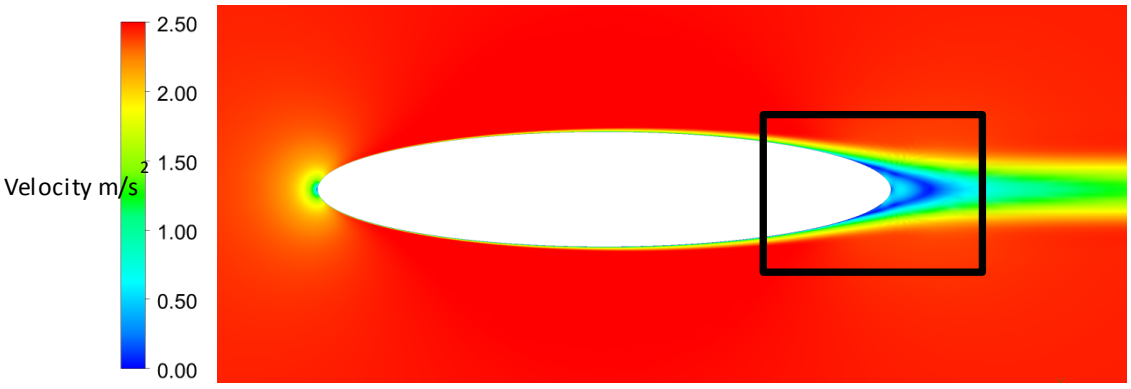

Figure 5: Flow velocity plot on symmetry plane (x-y plane) indicating the thicker portion of the boundary layer over the posterior of the spheroid and also the wake present on any real body.